AN EXPERIMENT IN LARGE-SCALE AIR-SEA INTERACTION

by

DANIEL GOLAN

B.S., State University of New York at Albany
(1976)

SUBMITTED IN PARTIAL FULFILLMENT
OF THE REQUIREMENTS FOR THE
DEGREE OF

MASTER OF SCIENCE

at the

MASSACHUSETTS INSTITUTE OF TECHNOLOGY

October, 1979

Signature of Author ....
Department of Meteorology,
October 1979

Certified by ....
Thesis Supervisor

Accepted by ....Lindgren................................
Chairman, Departmental Committee
on Graduate Students

AN EXPERIMENT IN LARGE-SCALE AIR-SEA INTERACTION

by

DANIEL GOLAN

Submitted to the Department of Meteorology
on October 2, 1979 in partial fulfillment of the requirements
for the Degree of Master of Science

ABSTRACT

Parsons' (1969) two-layer, wind-driven, steady-state, mid-latitude, β -plane ocean model is used as the principal component in a study of oceanic heat transport. Parsons' solution for the flow in the upper layer is combined with a solution for the flow in the directly-driven lower layer to give the surface layer flow everywhere in the basin. Fixed distributions of atmospheric wind stress and surface level atmospheric temperature are applied at the top boundary of the ocean. Heat is presumed to flow across the air-sea interface as a linear function of the difference between the anemometer level atmospheric temperature and the sea surface temperature. This heat is assumed well mixed in a surface oceanic mixed layer whose distribution is specified and held fixed and whose mean depth is taken to be 100 m.

Given a value of the magnitude of the fixed distribution of wind stress, and steady-state ocean circulation is calculated. The oceanic mixed layer thermodynamic equation

is then integrated to equilibrium as an initial value problem. A Lagrangian method in which parcels are followed around streamlines with the flow with heat being added according to the air-sea temperature difference is employed. The equilibrium distribution of vertical heat flux at the air-sea interface is derived from the atmospheric and equilibrium oceanic temperature distributions and the vertical heat flux law. The northward flux of heat across latitude walls in the basin is calculated.

The sensitivities of the oceanic temperatures and fluxes to the wind stress driving, constant of proportionality in the linear heat flux law, and north south temperature difference of the zonally symmetric atmospheric temperatures are determined. Comparisons are made of model results with observations.

Thesis Supervisors: Titles:

Jule G. Charney   Sloan Professor of Meteorology

Glenn R. Flierl   Professor of Oceanography

TABLE OF CONTENTS

LIST OF FIGURES

LIST OF TABLES

I. Introduction

Recent findings have stimulated work on the oceans' role in climate dynamics. Results of data analyses (Vonder Haar and Oort, 1973; Oort and Vonder Haar, 1976) and calculations with complex global numerical models (Manabe et al., 1975; Bryan et al., 1975) suggest that the poleward oceanic heat transports are an important component of the global energy budget.

A major portion of the northward transport of heat by the ocean is the heat transported by the wind-driven circulation in the upper ocean. Large-scale horizontal ocean circulations forced by atmospheric winds transport water laterally in rotational circulations. As the water circulates its characteristics are modified through inter-actions with the surface layers of the atmosphere.

In the northward branch of the oceanic flow pattern tropical water is exposed to decreasing atmospheric temper-atures above. This situation leads to cooling of the ocean surface and warming of the lower atmosphere by an upward turbulent flux of heat from the ocean. In the southward branch of the gyre cold northern water is modified through exposure to the progressively warmer air above, with cooling occurring in the atmosphere and warming taking place at the surface of the ocean.

About the upper 100-200 m of the ocean undergo a seasonal

temperature cycle. This is about an order of magnitude more
mass than in the entire atmosphere. Due to the substantially
greater specific heat of water as compared to air as well as
the differences in mass involved, the atmosphere responds
much more quickly than the ocean to the annual cycle in
solar forcing. As will be seen below, however, the response
of the ocean surface temperature to the seasonal forcing
cycle is noteworthy.

We present in Figs. 10a and 10b observed March and
August mean sea surface temperatures from the U.S. Naval
Oceanographic Atlas of the North Atlantic Ocean. The most
outstanding feature of the March distribution is the intense
front which exists off the North American coast from Cape
Hatteras to Nova Scotia. Seaward of this front is a region
in which the isotherms are strongly bowed to the north. In
the interior of the ocean the temperature pattern is pre-
dominantly zonal with gradients much weaker than near the
coastlines. Near the African coast there is a sharp
intrusion of cold water to the south.

The August distribution of sea surface temperatures
is similar in many respects to the March distribution, but
there is a notable discrepancy. With the exception of the
area westward of the British Isles, there is a general
decrease in the meridional temperature gradient from the
winter case. This effect is most pronounced in the southern
half of the North Atlantic and near western boundaries.
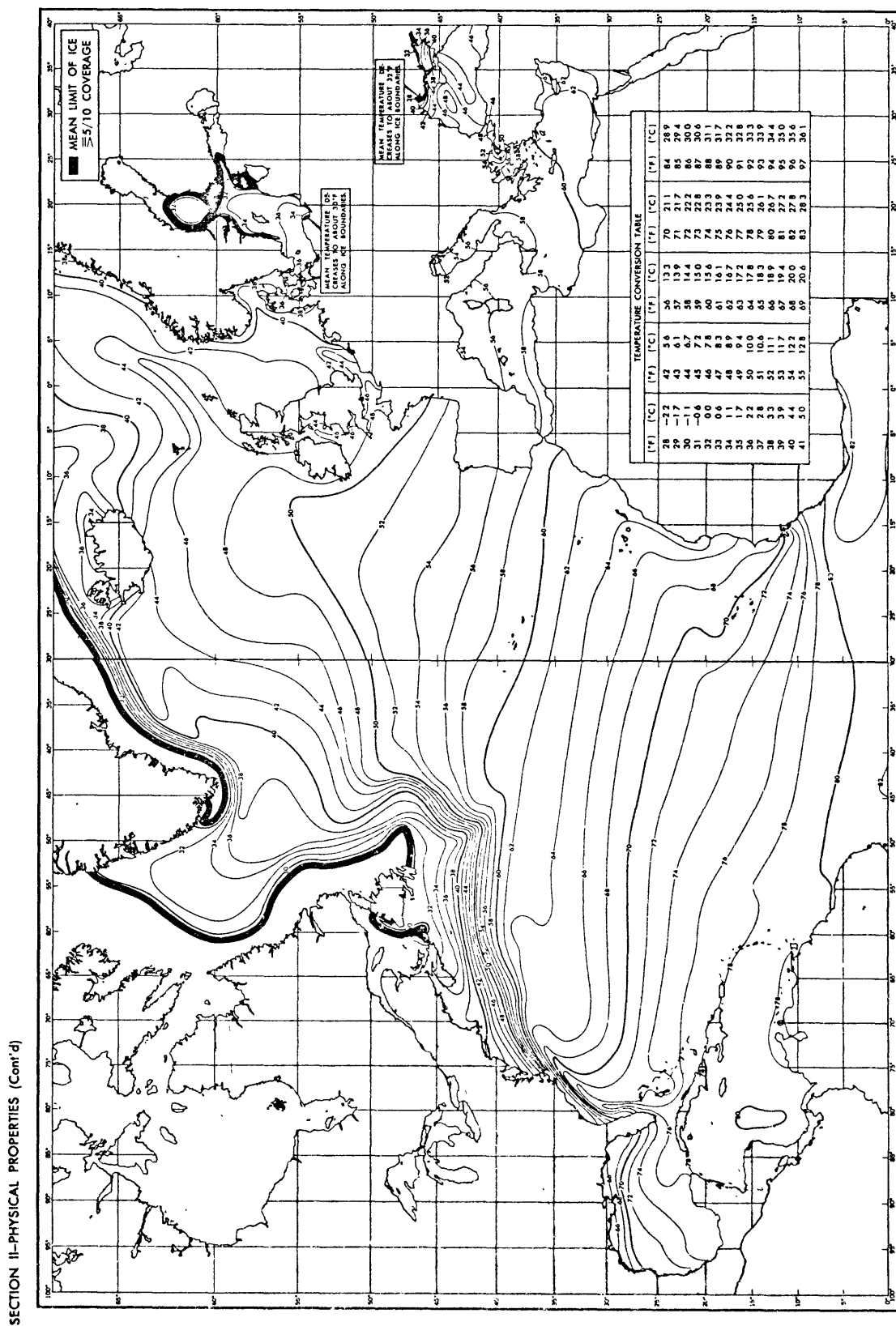
Fig. 10a. Mean March Sea-Surface Temperature in °F (from U.S. Naval Oceanographic Atlas of the North Atlantic Ocean)
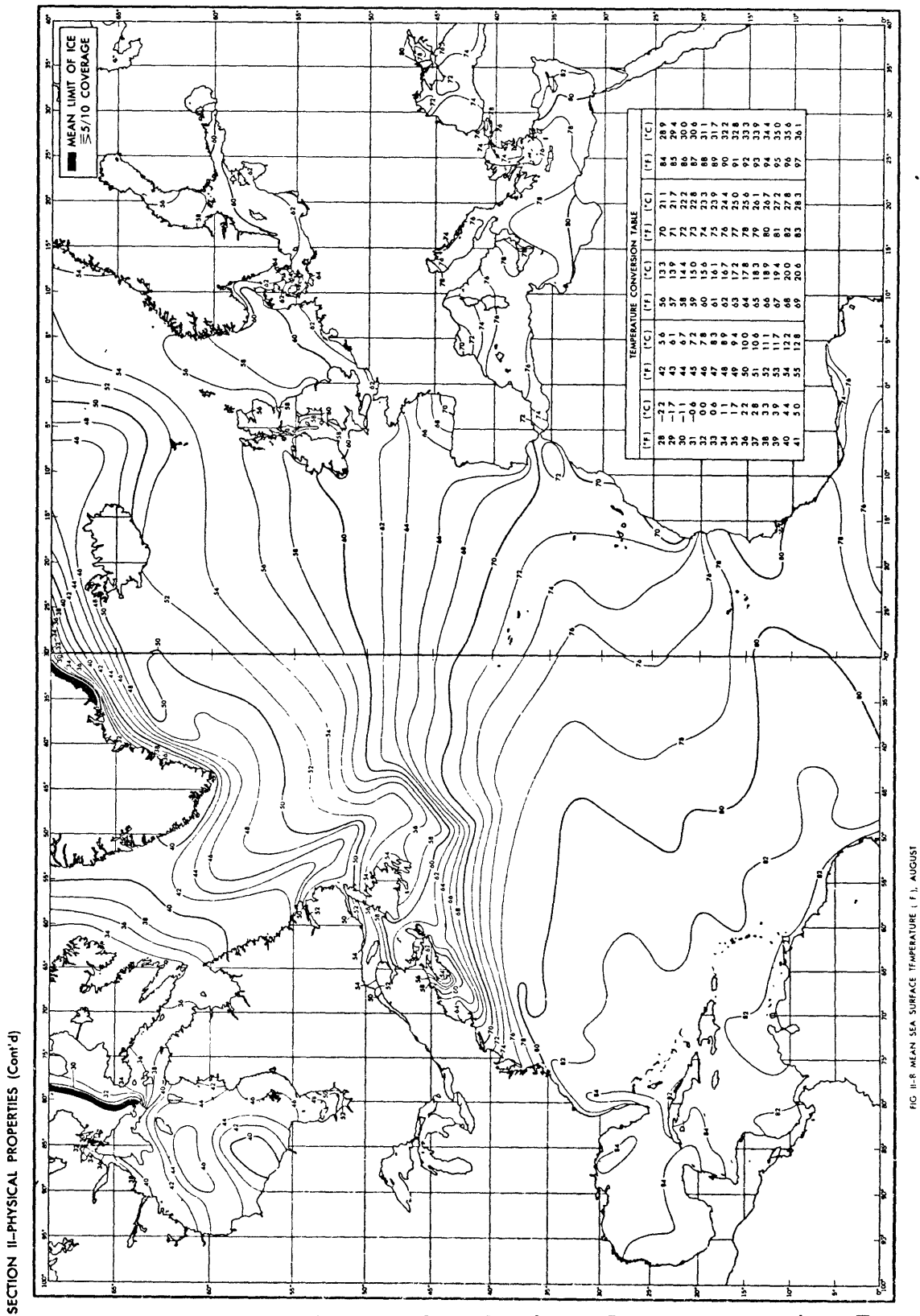
SECTION II—PHYSICAL PROPERTIES (Cont'd)

SECTION II—PHYSICAL PROPERTIES (Cont'd)

Fig. 10b. Mean August Sea-Surface Temperature in °F (from U.S. Naval Oceanographic Atlas of the North Atlantic Ocean)

On the extreme western side of the ocean the August pattern is quite similar in shape, not strength, to that existing in March. We see a front that is still fairly strong bordered on its southeastern side by a tongue of warm water protruding past Cape Hatteras. On the extreme eastern side of the ocean there is again a southward intrusion of cold water, although not as sharp.

The most dramatic disparity between the two maps occurs in the interior in the southeastern region. A zonal temperature gradient is present in the August distribution which replaces the essentially meridional March gradient. This dramatic seasonal shift in the mid-Atlantic sea surface temperature distribution has not been satisfactorally explained.

Bunker and Worthington (1976) have used bulk aero-dynamic exchange equations to compute the vertical flux of energy through the surface of the North Atlantic Ocean for a 32 year period. Their study is the most detailed of its kind as they had access to a much more complete set of surface marine observation than was previously available. The dependence of the exchange coefficients on wind speed and air stability were included in the calculations. Fluxes were calculated from individual observations of wind and temperature and then averaged.

Fig. 12b shows the resulting distribution of the net heat gain of the North Atlantic Ocean expressed in units of
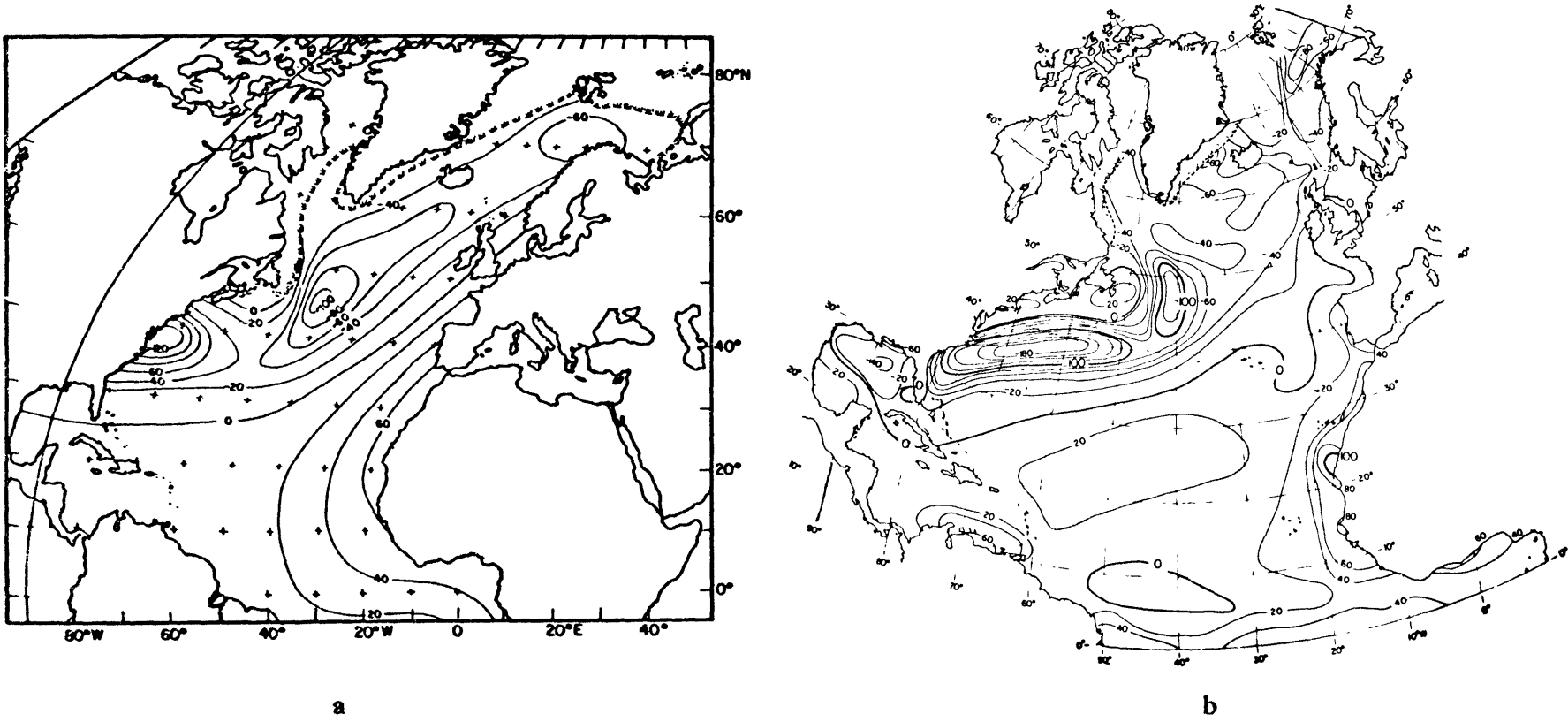
a   b

Fig. 12.   Vertical Heat Flux for North Atlantic,
            a. from Budyko (1963)   b. from Bunker & Worthington
                                        (1976)

kcal cm^{-2}yr^{-1}. It is seen that the largest negative value is in the region of the Gulf Stream where there are stong losses of heat in winter. The cold returning current in the interior of the ocean experiences a relatively mild warming. Fig. 12a shows results of a similar calculation by Budyko (1963).

The results presented in Figs. 10 and 12 are strongly coupled. Immediately northward of the axis of greatest heat loss to the atmosphere is the intense front in the sea surface temperature field. In the region of mild vertical heat flow in the interior of the ocean the temperature field is much flatter. Regions of high positive values of the heat flux near the west coast of Africa are also regions of strong oceanic temperature gradients.

In the interest of gaining a better understanding of the mechanisms by which our present climate is shaped and with the long-term goal being climate prediction, more must be known of global air-sea interaction. We will look for the equilibrium response of an ocean model to a number of fixed external conditions.

II. The Model

This paper reports a study of limited air sea inter-
action with a simple model. Attention is directed to the
thermal response of an idealized ocean model to a given
atmospheric state. The ocean is allowed to transport heat
in the wind-driven surface layers. Transport processes
across the ocean-atmosphere interface are crudely para-
meterized. Changes in the oceanic state are not allowed
to feed back on the atmosphere.

The ocean model is based on Parsons' (1969) study of
Gulf Stream separation. There he considered a two-layer,
wind-driven, steady-state, mid-latitude β-plane ocean within
a square basin. The geometry of the model is presented
in Fig. 1. We will consider the southern and northern
walls to correspond roughly to 10°N and 50°N. The two
immiscible layers of fluid are homogeneous and incompressible;
the lower layer is of slightly greater density than the upper
layer ($\rho_{LL} \gtrsim \rho_{UL}$) and has five times as much mass. Pressure
is assumed hydrostatic and the lower layer fluid is assumed
inert except when directly driven by the wind in the situ-
ation where upon layer fluid does not completely cover the
basin. The horizontal components of the velocity are assumed
uniform within the layers. Friction is modeled as an inter-
facial drag proportional to the upper layer velocity and as
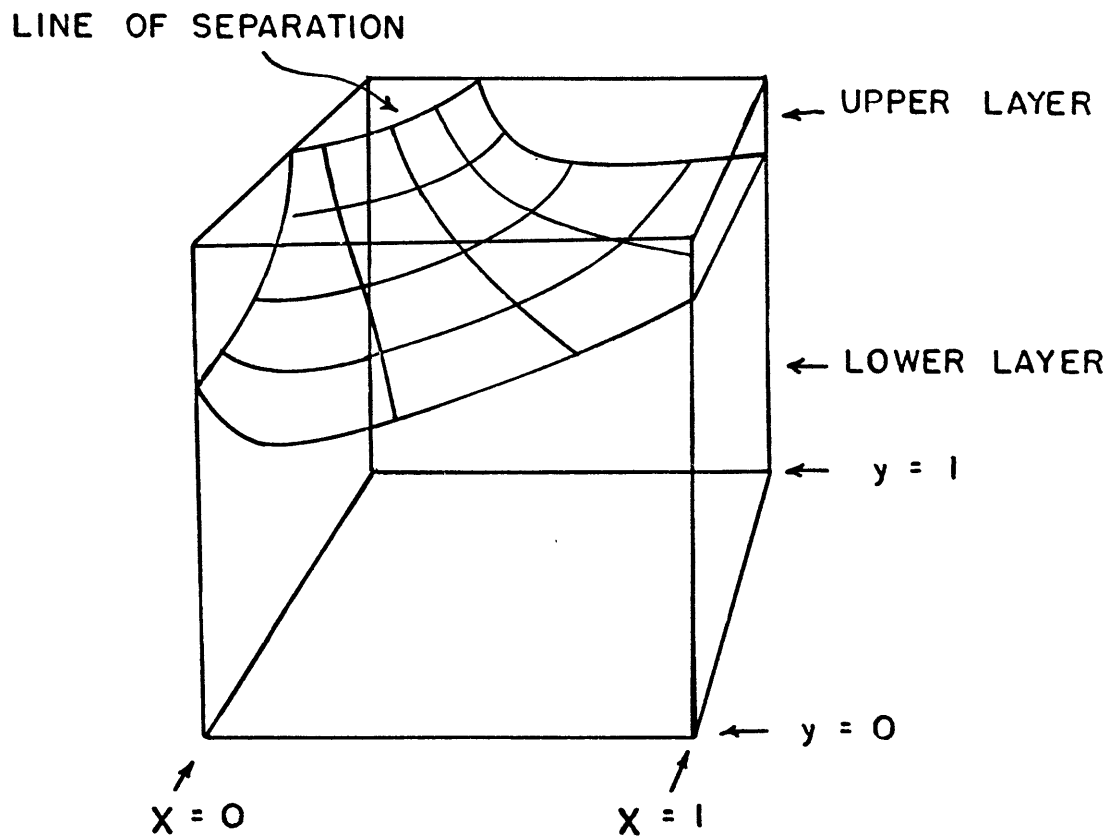bottom friction in the case of the directly-driven lower layer.

Fig. 1. Schematic of Model

For the upper layer, the vertically integrated equations of motion and mass continuity are:

$$D(\underset{\sim}{u} \cdot \nabla)\underset{\sim}{u} + f\,\hat{k} \times D\underset{\sim}{u} = -g' D\nabla D + \tau/\rho_0 - K\underset{\sim}{u} \qquad (1)$$

$$\nabla \cdot (D\underset{\sim}{u}) = 0 \qquad (2)$$

D is the upper layer depth, $\underset{\sim}{u} = (u, v)$ is the horizontal velocity vector with Cartesian components in the eastward and northward directions, respectively. f is the Coriolis parameter, taken as a linear function of latitude in the β -plane approximation, $g' = g(1 - \rho_{uL}/\rho_{LL})$ is reduced gravity, g is actual gravity, K is a drag coefficient. $\underset{\sim}{\tau}$ is the wind stress which we will assume to be in the zonal direction, i.e., $\underset{\sim}{\tau} = (\tau_x, 0)$. We will further fix the stress distribution to be $\tau_x = -W\cos(y/L)$ with W variable. The equations for the directly-driven lower layer are analogous with the variables taking on their lower layer values and reduced gravity being replaced by actual gravity.

The equations are non-dimensionalized with scales characteristic of variations over the length of the basin. We will assume that the Rossby number is small and will therefore discard the inertial terms. The result is the following set of equations expressed in terms of an upper layer transport streamfunction:

$$-f\frac{\partial \psi}{\partial x} = -D\frac{\partial D}{\partial x} + \frac{\epsilon}{D}\frac{\partial \psi}{\partial y} + \lambda \, \Upsilon_x \qquad (3)$$

$$-f\frac{\partial \psi}{\partial y} = -D\frac{\partial D}{\partial y} - \frac{\epsilon}{D}\frac{\partial \psi}{\partial x} \qquad (4)$$

ψ is defined by $\qquad D\underset{\sim}{u} = -\hat{k} \times \nabla \psi \qquad (5)$

$\epsilon = {}^K\!/_{\beta L d}$ is a non-dimensional friction parameter and $\lambda = {}^{LW}\!/_{g'\rho d^2}$ is a non-dimensional wind stress parameter. d is the mean upper layer depth and L is the length of the basin.

The system is solved using boundary layer techniques. The frictional terms are assumed small outside of narrow boundary layer regions. The total amount of water in each layer is constant. As a result, if the curl of the wind stress is large enough, the deepening of the thermocline in the center of the basin may force the withdrawal of upper layer water from the shallowest region - the north-west corner of the basin. Vorticity balance in the boundary layer between the advection of planetary vorticity and the frictional input of vorticity can only be achieved if the boundary layer is on the western side of the ocean. Our scaling has presupposed the boundary layer to be frictionally controlled.

The equations for the boundary layer are found by scaling east-west variations by the boundary layer thickness ϵ . The frictional and wind stress terms in the first equation are found to be relatively small in this region.

Thus, geostrophic balance holds for the flow parallel to the boundary. All three terms are of comparable magnitude in the second equation.

The boundary conditions are no normal flow through solid walls. The interior solution is a broad anticyclonic gyre with eastward flow in the upper half, westward flow in the lower half and a southward component to the flow everywhere. By continuity, all of the flow in the interior has to be returned to the north in the western boundary layer.

The phenomenon of separation in the model can be interpreted as a breakdown of the circulation which occurs when the wind stress is turned on strong enough that the Sverdrup transport in the interior becomes too large to be returned by the western boundary layer, which scaling shows to be geostrophic. For geostrophic balance to continue to hold, the upper layer depth at the western coast must become negative. To avoid this we require that the boundary layer separate from the coast at the latitude where the depth goes to zero. This effectively limits the area of the interior which is acted on by the wind stress and reduces the south-ward interior flow to the point at which it can just be accomplished geostrophically by the separated current.

The mathematical analysis of the model results in three asymptotically valid solutions. The regions of their validity are the western boundary layer, the separated boundary layer and the region to the south and east of these.

A uniformly valid approximation to the solution may be
obtained by combining the asymptotically valid solutions
with formulas of the form

$$X_{unis} = X_{bl} + X_{int} - X_{match} \qquad (6)$$

where X_{match} represents the limit of either the interior
or the boundary layer solution as it leaves its region of
validity.

Conservation of mass in the upper layer gives a
condition which allows determination of the upper layer
depth at the eastern wall.

$$I = \iint D(x, y, h, \lambda) \, dx \, dy \qquad (7)$$

Extending Parson's work, we will derive a separate
solution for the flow in the directly-driven lower layer in
the northwest corner of the basin. The streamfunction is
assumed zero on the lower layer side of the line of separ-
ation - no momentum transfer is allowed to the inert lower
layer covered by the upper layer. This assumption is
motivated by a study by Kamenkovich and Reznik (1972) in
which the streamfunction was allowed to vary at the
surfaced interface in a similar two-layer model. They
found that the lower layer flow diminished very rapidly with
distance from the line of separation in the region where

the upper layer exists. Veronis (1973) has used a similar assumption in his study of the world ocean circulation.

A western boundary layer is required to return the Sverdrup flow in the directly-driven lower layer. The velocities here are much smaller than in the upper layer due to the greater depth of fluid, larger effective gravity and the small wind stress curl near the northern boundary. These factors also preclude separation of the lower layer western boundary layer from the coast for reasonable stress magnitudes. The solutions in each of the five regions are given in the Appendix.

It should be stated that use was made of Parsons' circulation model not because it incorporates state-of-the-art understanding of ocean dynamics. It does not. Parsons' choice for the force balance in the boundary layers in which the frictional terms dominate the inertial terms is not realistic for large-scale oceanic flows. In the real ocean the inertial forces seem to be dominant. There is also an inconsistency in the model in which the submerged lower layer receives no momentum transfer from the layer above, despite the interfacial friction which is assumed to act on the upper layer. A similar inconsistency exists in the manner in which we model the flow in the directly-driven lower layer by not allowing lateral transfers of momentum across the line of separation. The effect of the energetic

mesoscale eddy field on the large-scale dynamics has also
not been included.

While acknowledging these limitations, it is felt that
the ocean model is sufficiently realistic to give an adequate
representation of the flow in the real ocean. It captures
the concentrated northward currents near the western
boundaries and the contrasting slow southward interior
flows. These features are essential to the ocean's heat
transporting capability. Use of a more sophisticated model
of ocean dynamics would affect details of the equilibrium
ocean temperature patterns but not the qualitative nature
of the processes which force these patterns.

Attention is confined to the effects of the wind-driven
surface circulation in the horizontal transport of heat.
Other mechanisms of heat transport will be neglected. It
will be necessary to model the vertical transport of heat
across the air-sea interface. A mechanism must also be
postulated to distribute the heat within the ocean.

Allowance for the transfer of heat between the atmosphere
and the ocean will be made by postulating a linear heat
transfer law. The heat transport into the ocean will be
assumed proportional to the difference between the fixed
surface level atmospheric temperature and the ocean temperature.

This parameterization is motivated by a study by
Haney (1971) in which he proposed a similar form for an
ocean model surface thermal boundary condition. Haney

conducted a heat budget analysis of the ocean surface
appropriate to zonally and time averaged atmospheric
conditions. His parameterization takes into account solar
radiation, net longwave radiation and sensible and latent
heat fluxes. It can be expressed as a linear law if the
atmospheric temperature is replaced by a slightly higher
effective atmospheric temperature to include the effects
of solar radiation and atmospheric moisture on the flux.

Through an analysis of observations he arrives at a
value of the coupling coefficient which slowly varies with
latitude and for the region we are considering (10°N - 50°N)
has a mean value of about 30,000 cal $cm^{-2}yr^{-1}°C^{-1}$. In a
later paper (Haney, 1975) he presents results of calculations
of the coupling coefficient presumably using different data
and arrives at a value of about 18,000 cal $cm^{-2}yr^{-1}°C^{-1}$.
Takano (1975) employs a similar parameterization and uses
a value of approximately 6000 cal $cm^{-2}yr^{-1}°C^{-1}$. Evidently,
an appropriate value of the constant is difficult to
determine. The law gives the proper direction of heat
flow and gives results which are easy to interpret.

Vertical heat transport within the ocean is modeled by
assuming this surface level of the ocean to be well mixed.
We will impose the condition that this surface mixed layer
be non-divergent so that there will be no advection of heat
out of the layer. This condition is satisfied by choosing
the mixed layer depth to be proportional to the thermocline

depth, or the lower layer depth where the upper layer is
absent. In the upper layer region just south of the line
of separation the mixed layer is quite shallow. This tends
to increase the ratio of vertical heat transfers to advection
and thus compensates to a degree for the increase in advection
in the region due to the high velocities near the line of
separation. Additionally, the base of the mixed layer will
not be allowed to conduct heat. The mean depth of the
mixed layer is taken to be 100 m.

The thermodynamic equation for the model ocean
vertically integrated over the depth of the mixed layer is:

$$\rho C_p h \frac{dT_0}{dt} = C_{HF} (T_A - T_0) \tag{8}$$

where C_p is the heat capacity of water, h is the mixed
layer depth, C_{HF} is a constant of proportionality, T_A is
the atmospheric temperature and T_0 is the oceanic temperature.

III. Numerical Solution

Numerical solutions to the model equations are obtained
in the following manner. Solutions will be found on a
square grid with variable resolution. Given values of the
wind stress parameter λ , the fixed distribution of wind
stress and the depth of the upper layer at the eastern wall h ,
the position of the line of separation between upper and
lower layer water is evaluated from Eq. C1 (in Appendix).
The gridpoints which are adjacent to the line of separation
are identified.

The values of the interior solution for the depth are
evaluated at all gridpoints in the upper layer from Eq. A2.
The interior solution for the streamfunction is evaluated
at all points not on the walls from Eq. A1. Similarly, the
western boundary layer solutions (Eqs. B1 and B2) are
calculated at the upper layer gridpoints.

Because the separated boundary solution is expressed
in terms of natural coordinates, its evaluation is not as
straightforward. For each gridpoint it is necessary to find
the point on the line of separation from which the normal
to the line of separation includes the gridpoint. The
interior value of layer depth at that point on the separation
curve is then calculated from Eq. C2, as is the normal
distance from the gridpoint to the separation curve. At
this point the values of the separated solutions for the

streamfunction and depth may be directly evaluated from Eqs. C3 and C4.

The three solutions are then combined to give uniformly valid approximations with the formula:

$$X_{unif} = X_{int} + X_{sBL} - X_{sBL\infty} + X_{wBL} - X_{wBL\infty} \qquad (9)$$

where $X_{sBL\infty}$ and $X_{wBL\infty}$ represent the values of the boundary layer solutions at an infinite distance from the boundary on the normal containing a given gridpoint.

Once the solutions in the different regions have been ascertained and combined to give the uniformly valid approximation at the gridpoints, the total depth of upper layer fluid must be calculated to see if it equals one in non-dimensional units. In general it will not and the depth at the eastern wall is adjusted, the circulation is reevaluated and the total amount of upper layer fluid is rechecked until self-consistency is found.

A similar procedure is carried out to find the uniformly valid solutions for the lower layer, except that there is no boundary layer at the line of separation so only interior (Eqs. D1 and D2) and western boundary solutions (Eqs. E1 and E2) must be considered. These are combined with formulas of the form of Eq. 6. The depth of the lower layer at the line of separation in the interior solution is taken to be equal to the sum of the mean depths of the upper and lower layers.

Solutions for the lower layer equations are found with the equations nondimensionalized using scales appropriate to the lower layer. The resulting streamfunction and depth fields were converted to the upper layer scalings for further unified treatment.

It is then possible to find the velocity field with a centered finite difference form of Eq. 5. As illustrated in Fig. 2, points which are less than a grid interval away from the line of separation in either the x- or y-directions or both must be treated separately with an interpolation method. For such points the x-distance (for north-south velocities) or y-distance (for east-west velocities) from the gridpoint to the line of separation is calculated and an interpolation is done to find the streamfunction an equal distance to the other side of the gridpoint. The calculated distance and streamfunction are then used in a finite difference velocity calculation centered at the gridpoint.

The narrowness and intensity of the boundary currents dictate a high degree of resolution on the western side of the ocean. For simplicity a uniform grid was used. Below we will describe the integration of the thermodynamic equation which will involve finding the time for a parcel to cycle around the basin on a given streamline. We determine the degree of resolution required in the model by examining the streamline traversal times as a function of
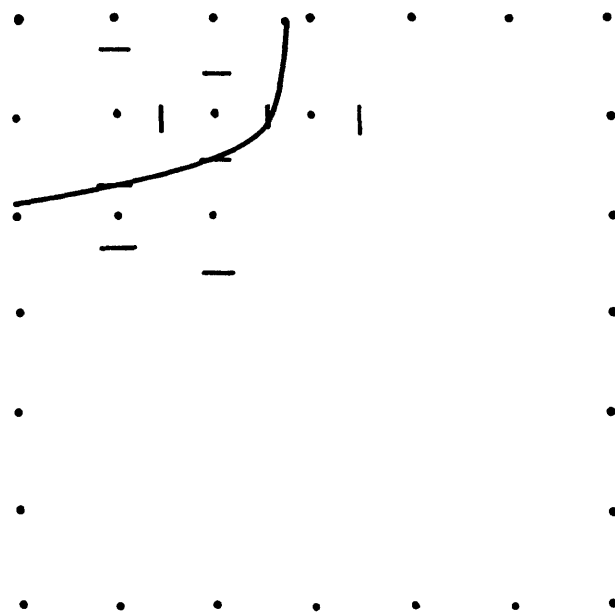
Fig. 2.   Interpolation for velocities near line of
          Separation

resolution. These are presented in Table 1.

As the resolution increases, the traversal times for
the individual streamlines decrease until the boundary
currents are adequately detected. Little noticeable
improvement occurs with resolutions greater than about 50
points in each direction (grid spacing of 120 km). For
the sake of economy the model was tested with the resolution
equal to 10. The cases presented in this paper were run
with a resolution of 50.

We have adopted values of the circulation parameters
presented by Parsons in his study. They are: mean upper
layer depth d of 300 m, length of basin L of 6000 km,
$\epsilon = 0.03$, $g = 1000$ cm s^{-2}, $g' = 2$ cm s^{-2}. We will consider
a broad range of wind stress parameters ($0.40 \le \lambda \le 0.80$),
a subset of those λ's considered by Parsons. In addition
$\lambda_{LL} = \lambda_{uL}/12500$ and $\epsilon_{LL} = \epsilon_{uL}/5$.

Fig. 3 gives the distribution of upper and lower layer
water at the surface for different values of the wind stress
parameter. As λ increases the thermocline depth increases,
the increased upper layer depth compensates for the loss of
upper layer area and mass conservation requires little
change in depth at the eastern wall.

The steady-state wind-driven ocean circulation is
shown in Figs. 4-6, a-c. Fig. 4 gives the mass transport
streamfunction. Fig. 5 gives the depth of the upper layer

TABLE 1

Traversal times in years for parcels on streamlines

used in temperature integration $(\lambda = 0.45)$

Resolution	10	20	30	40	50	60	70	80	90	100

Non-dimensional
Streamline Value

Upper Layer

	10	20	30	40	50	60	70	80	90	100
0.1	54.2	36.8	30.2	28.0	26.1	25.4	24.7	24.5	24.1	23.9
0.2	33.8	26.8	22.9	21.1	21.2	20.7	20.5.	20.3	20.1	20.2
0.3	25.6	21.7	19.6	18.4	18.6	18.4	18.1	18.1	18.1	18.1
0.4	23.8	18.5	16.6	16.7	16.6	16.5	16.4	16.5	16.5	16.5
0.5	20.3	16.1	15.7	15.0	15.1	15.2	15.0	15.1	15.2	15.1
0.6	17.2	14.4	13.9	13.7	13.6	13.7	13.8	13.8	13.8	13.8
0.7	14.7	12.6	12.0	12.4	12.3	12.2	12.5	12.6	12.5	12.7
0.8	11.7	11.1	11.1	11.2	11.3	11.0	11.1	11.2	11.5	11.5
0.9	10.4	8.7	9.3	9.2	9.9	9.8	10.1	10.0	10.2	10.1
1.0	7.6	8.1	8.3	8.6	8.4	8.6	8.7	8.7	9.0	8.9

Lower Layer

	10	20	30	40	50	60	70	80	90	100
0.04	210.	152.	127.	116.	111.	108.	102.	122.	102.	112.
0.08	115.	84.6	82.2	75.0	72.9	68.8	69.8	78.6	68.1	81.2
0.12	71.7	62.6	58.7	54.2	55.6	52.7	54.6	56.7	51.3	63.2
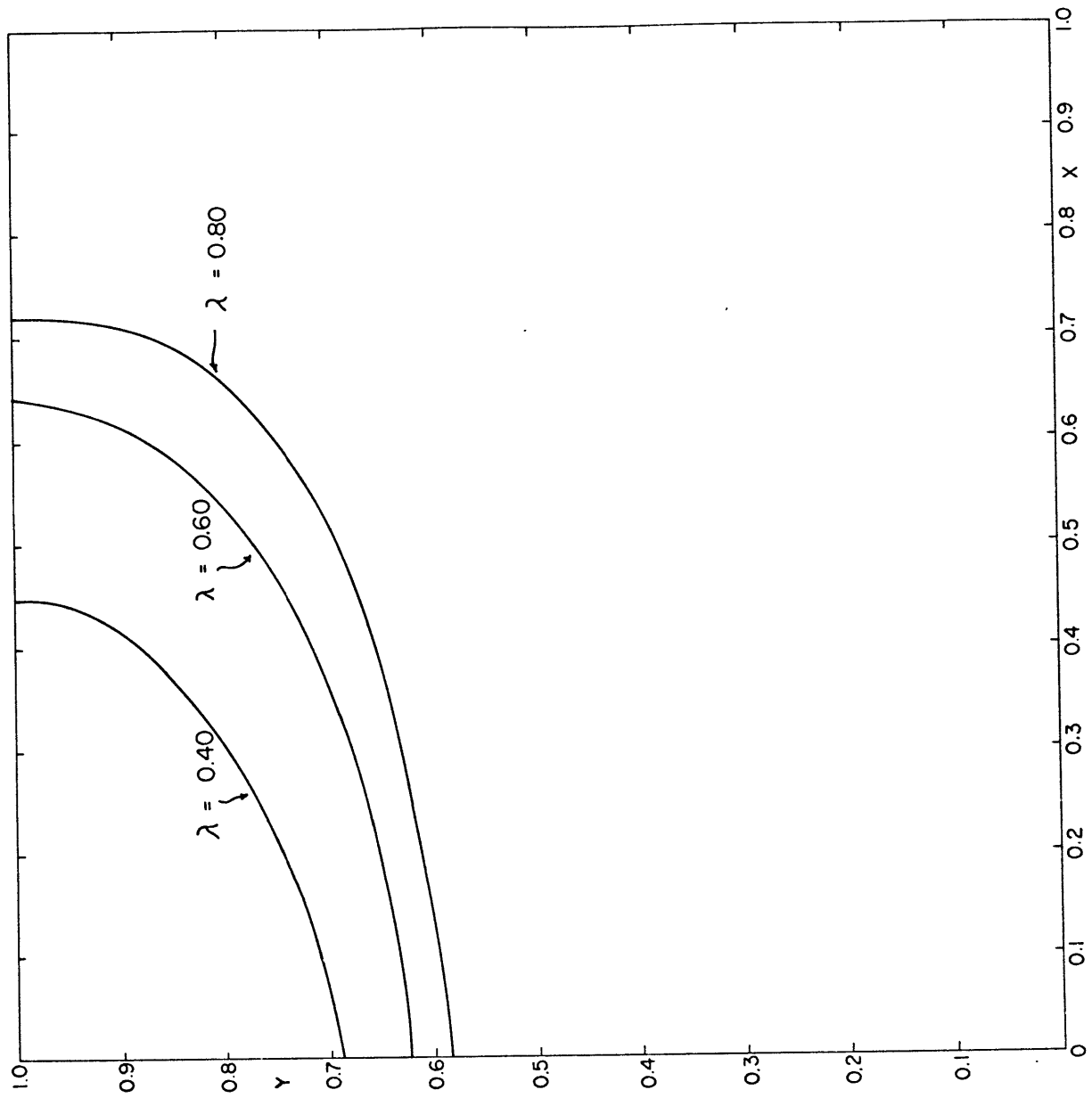
Fig. 3. Line of separation vs. λ
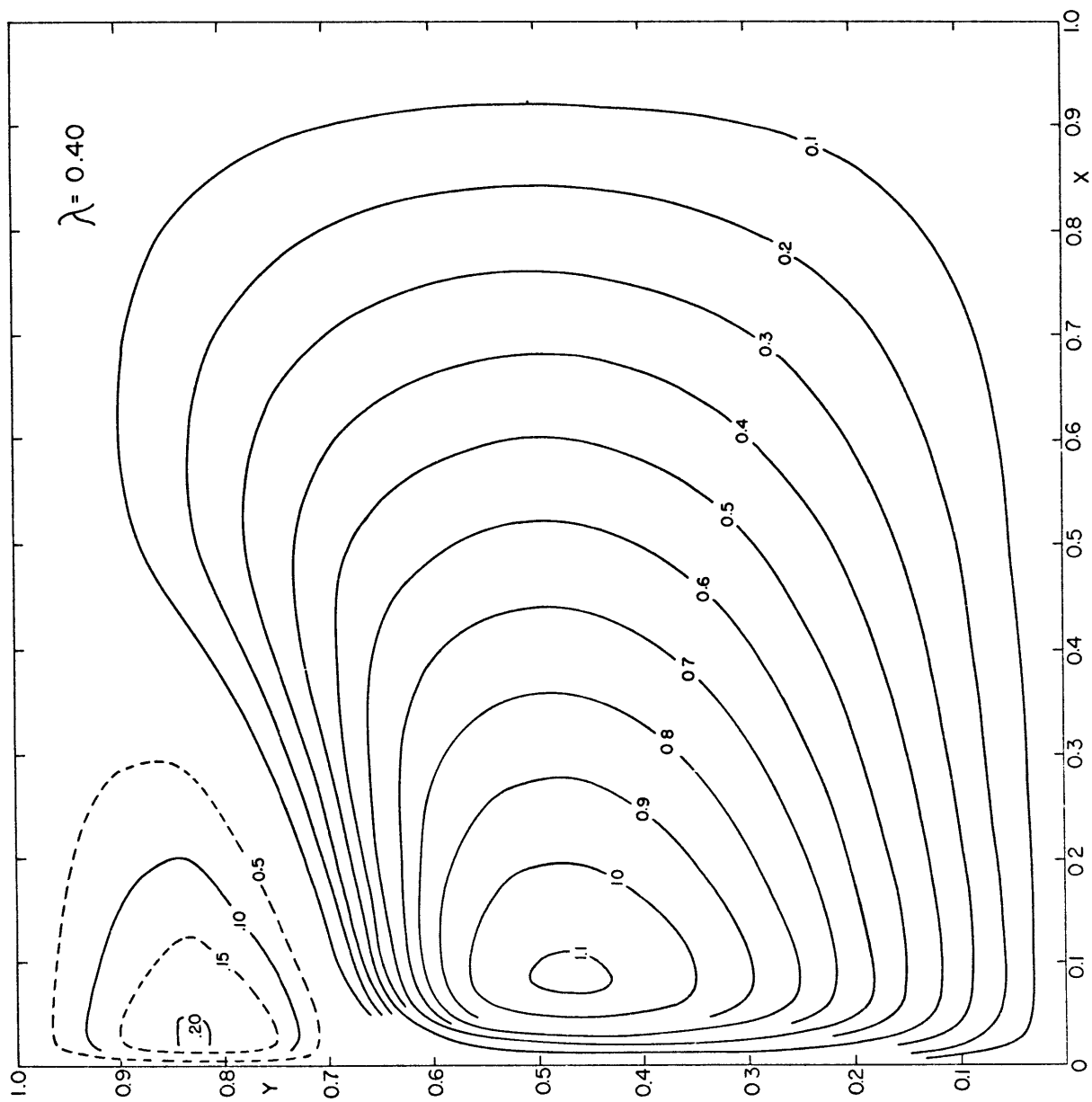
Fig. 4a. Non-dimensional Streamfunction (λ = 0.40)
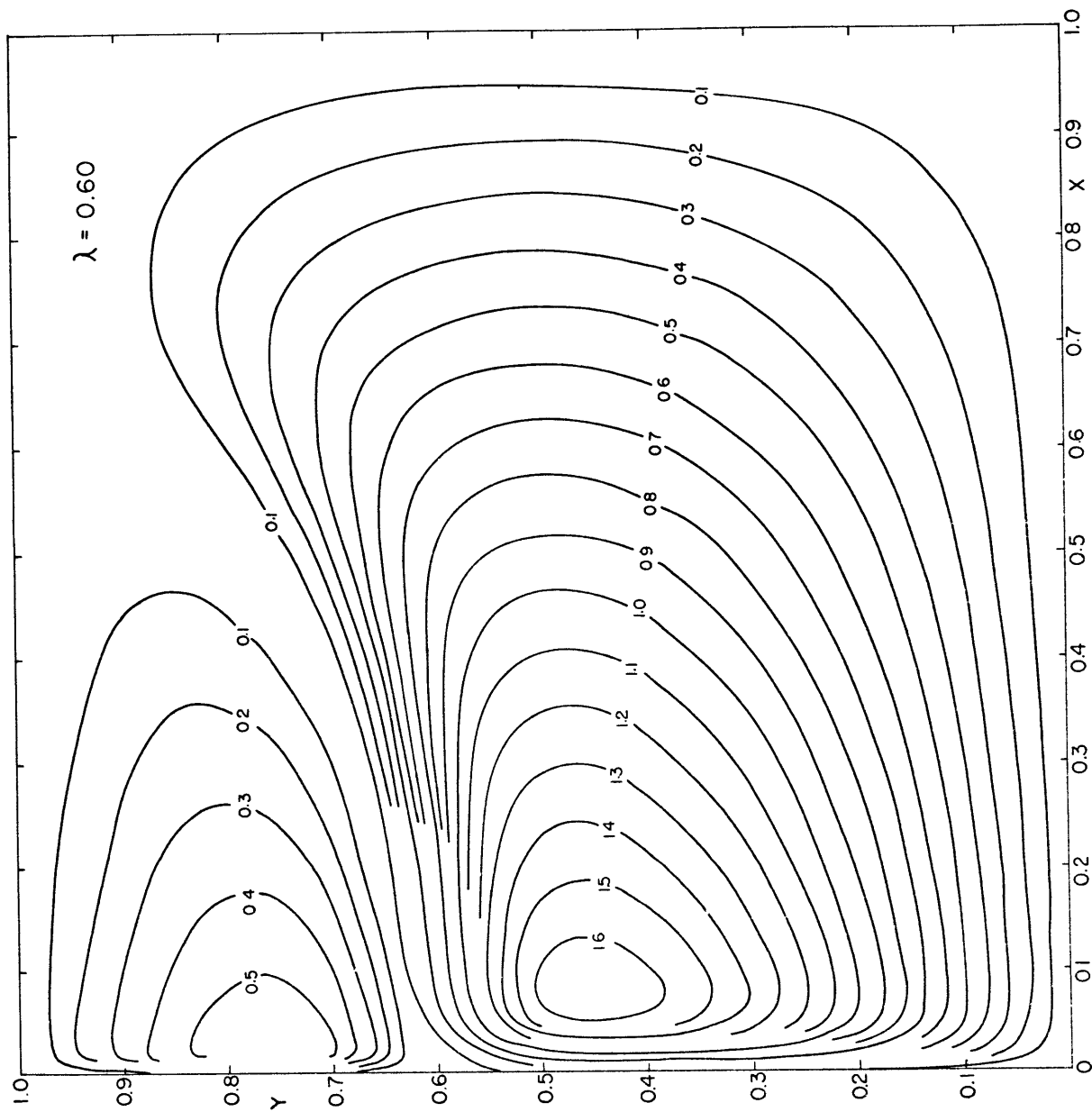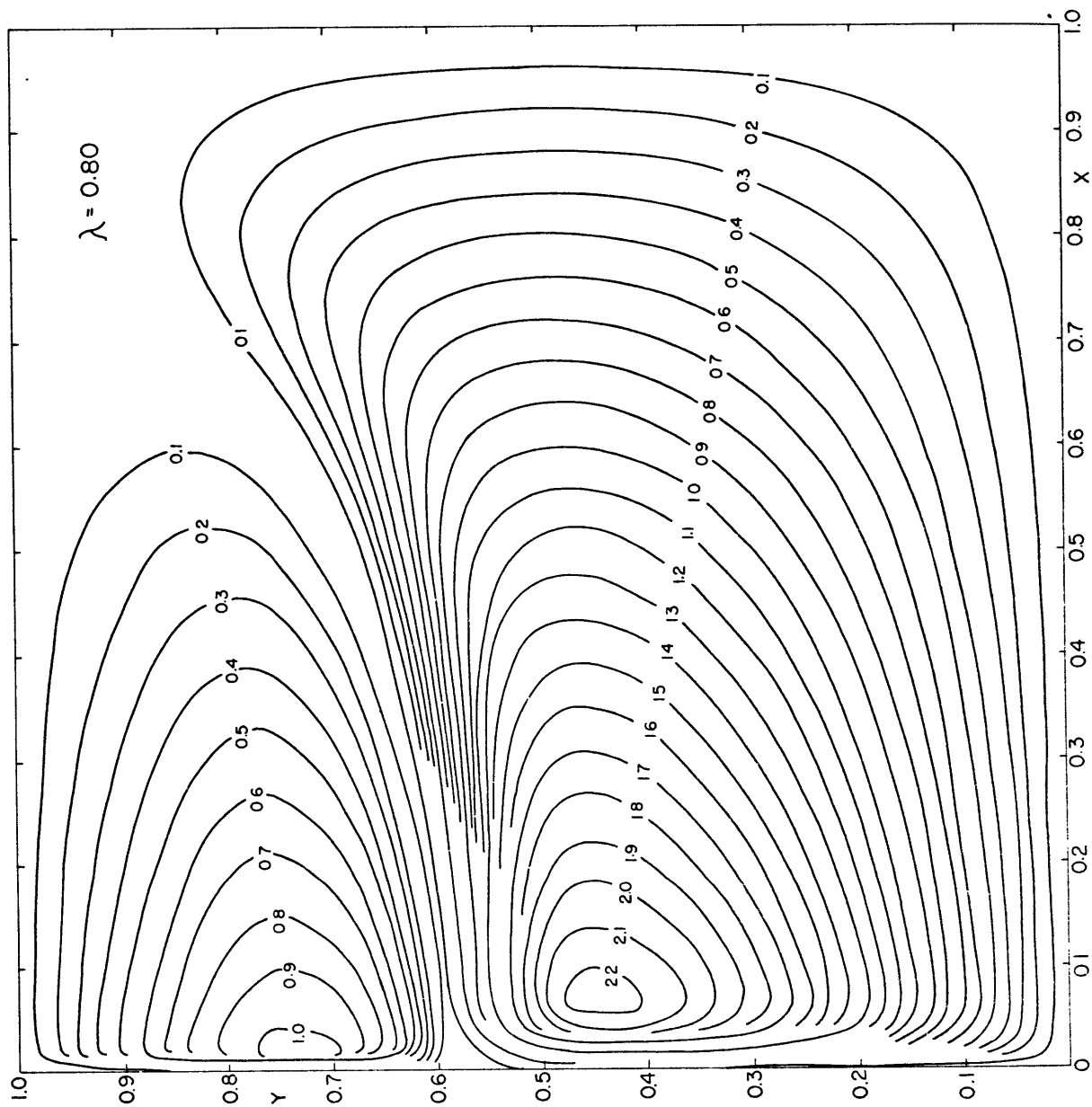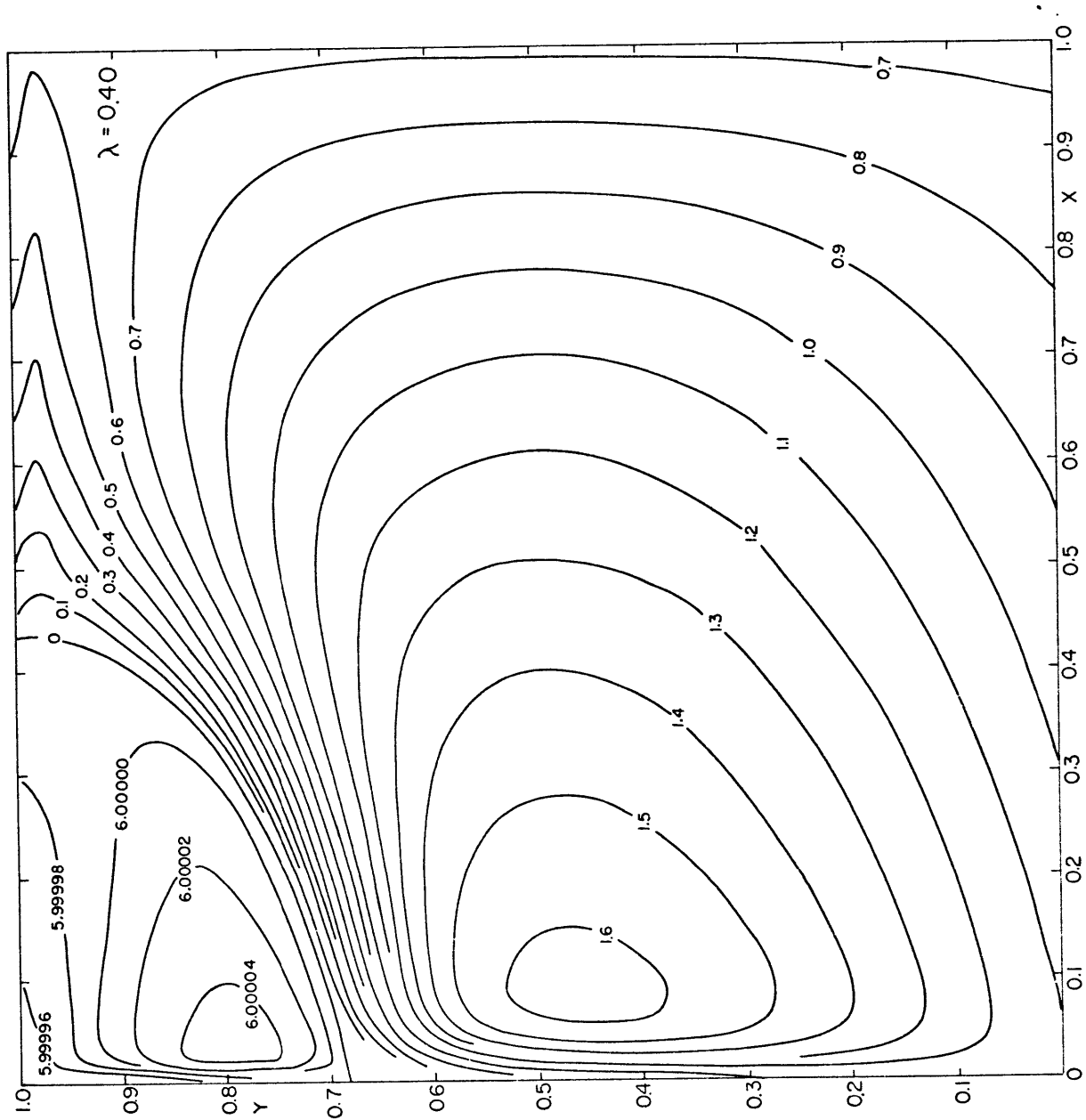
Fig. 4b. Non-dimensional Streamfunction ($\lambda = 0.60$)

Fig. 4c. Non-dimensional Streamfunction (λ = 0.80)

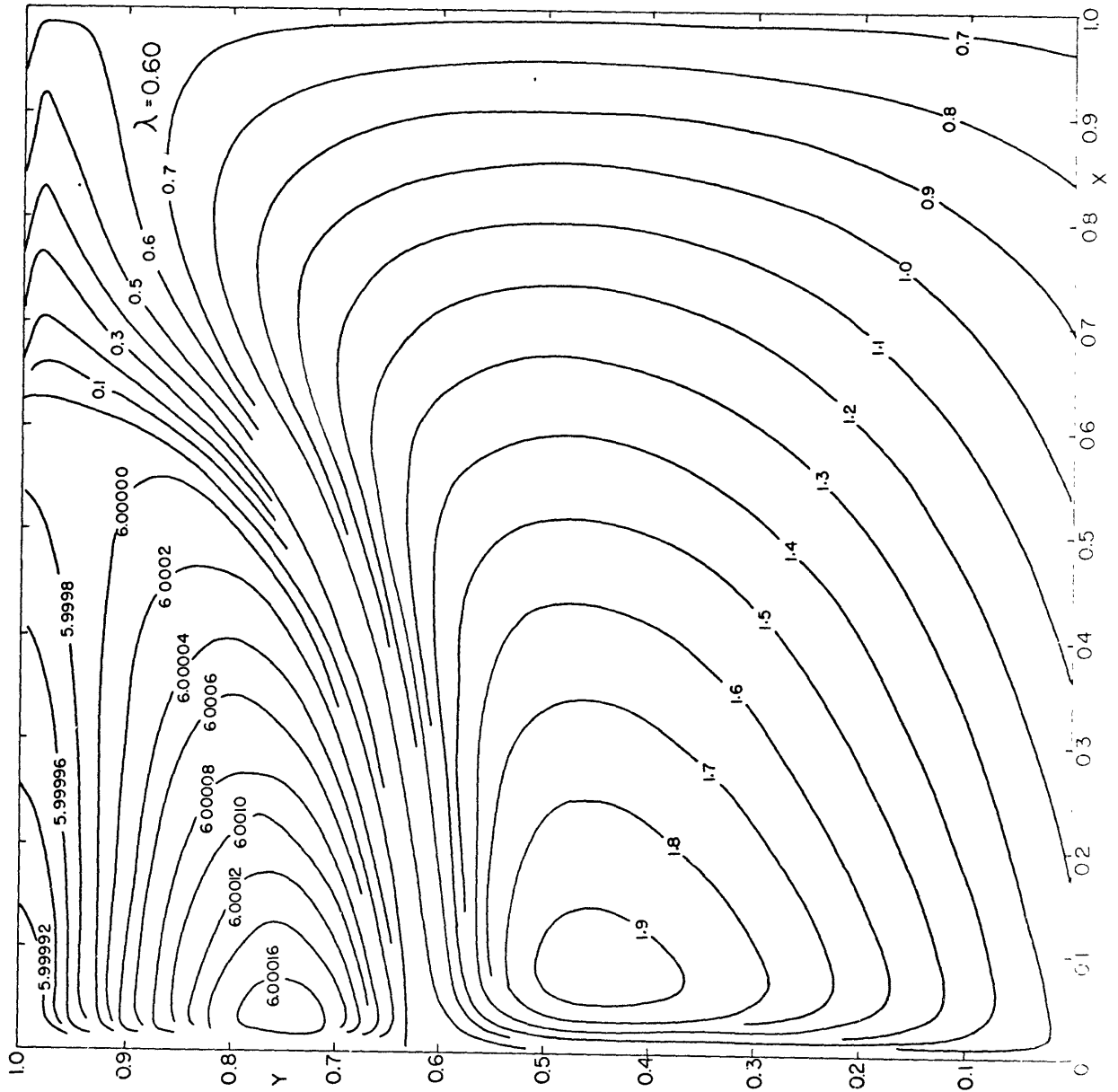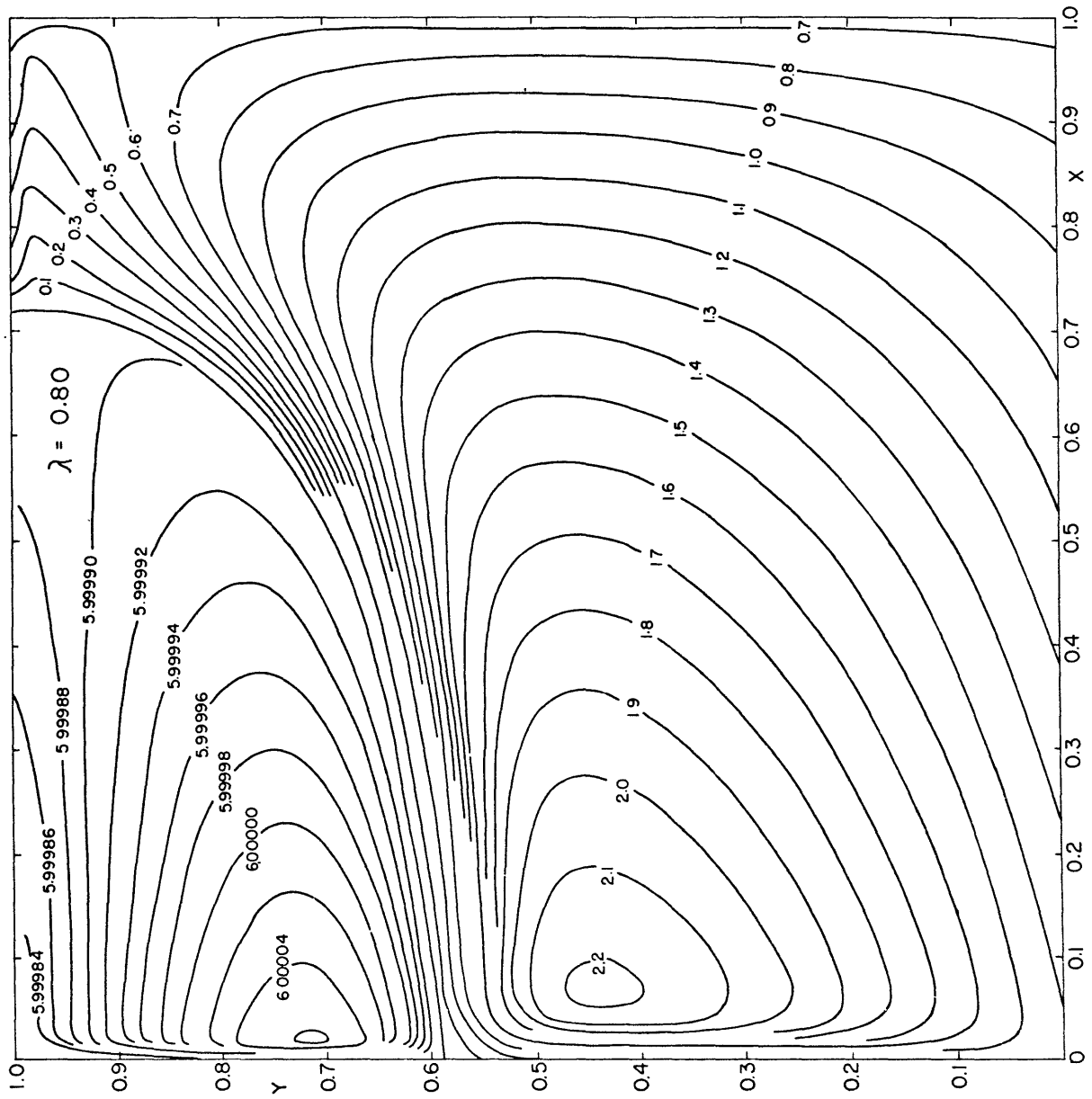Fig. 5a. Non-dimensional Surface Layer Depth (λ = 0.40)

Fig. 5b. Non-dimensional Surface Layer Depth (λ = 0.60)

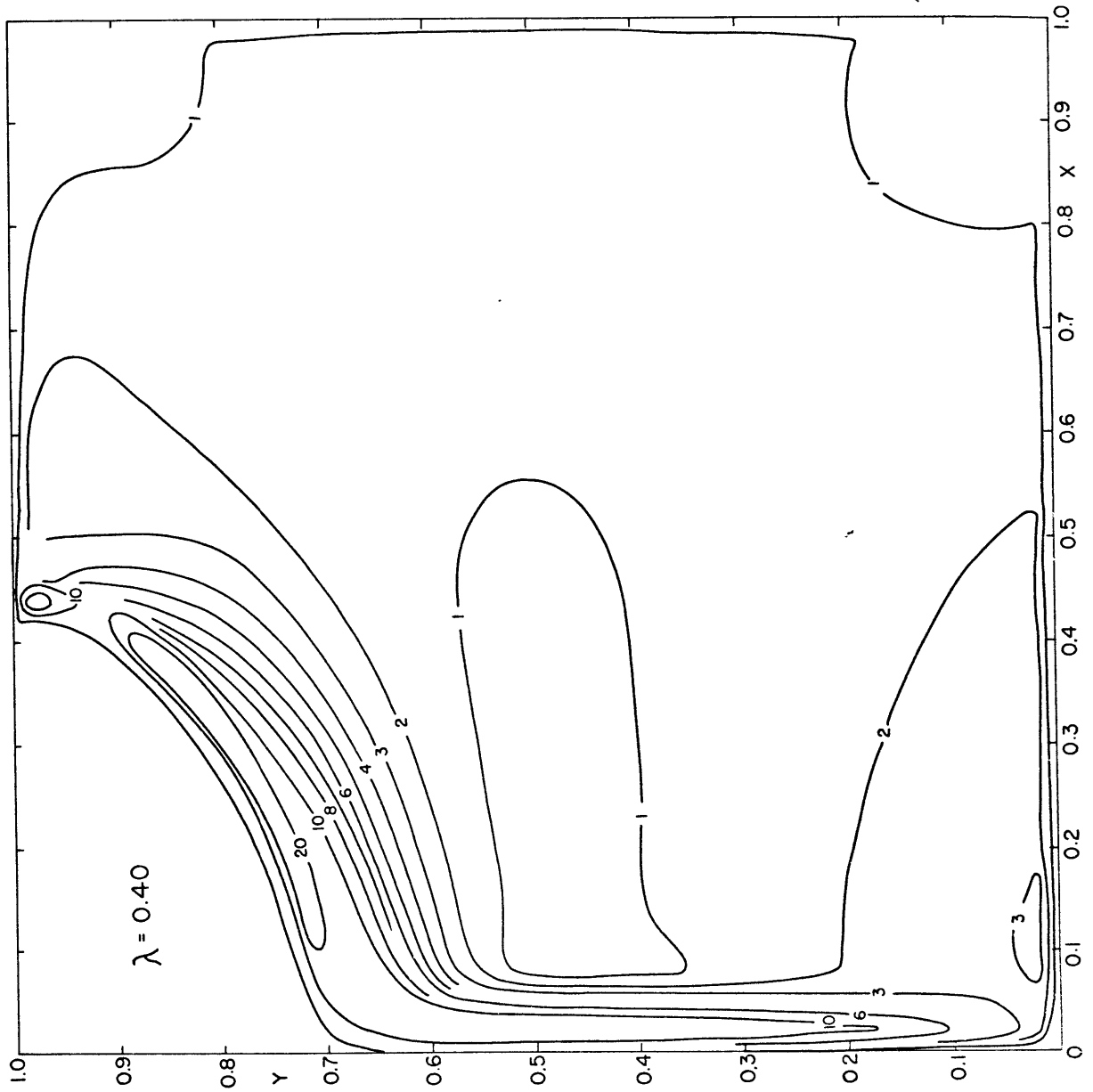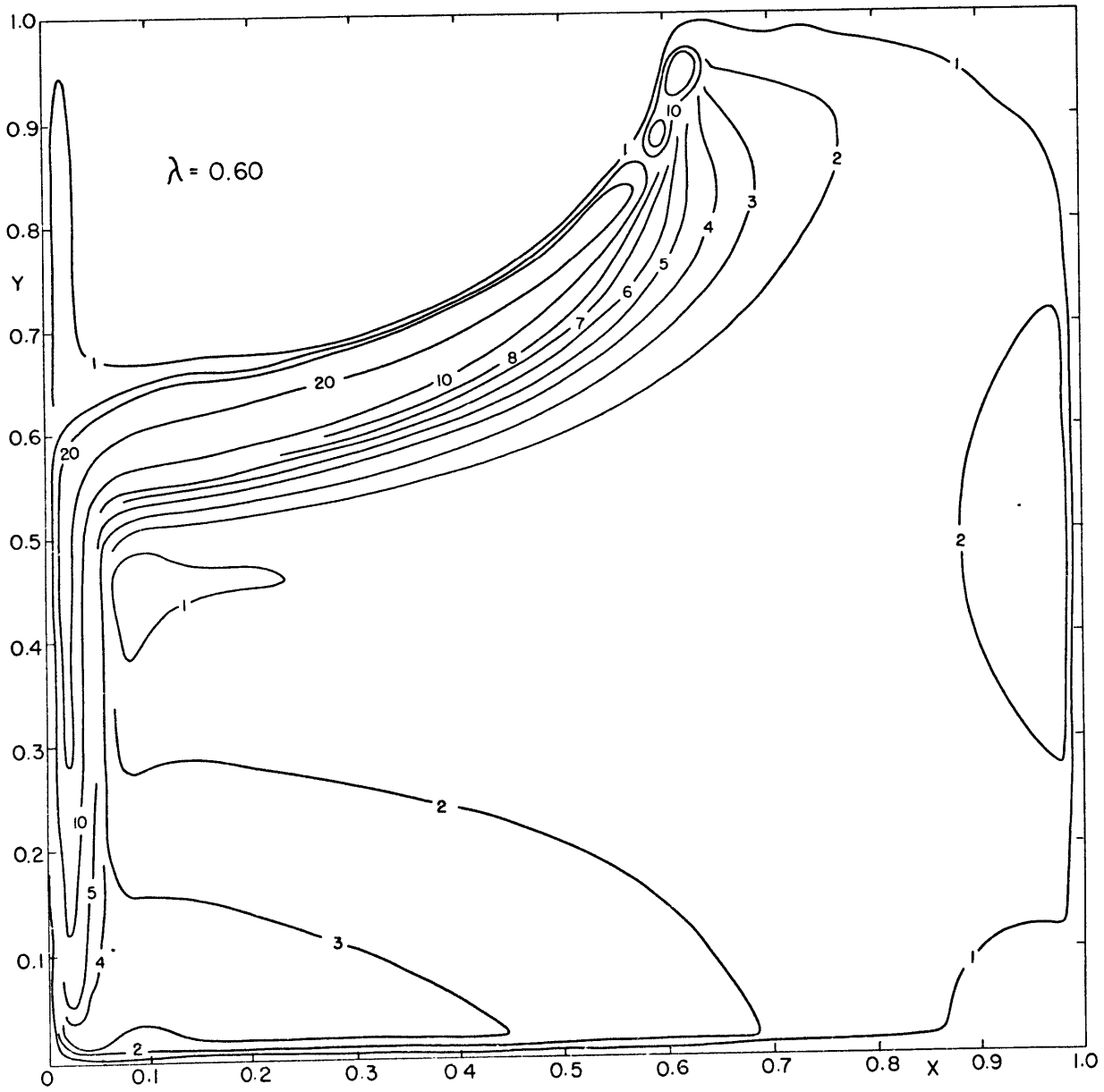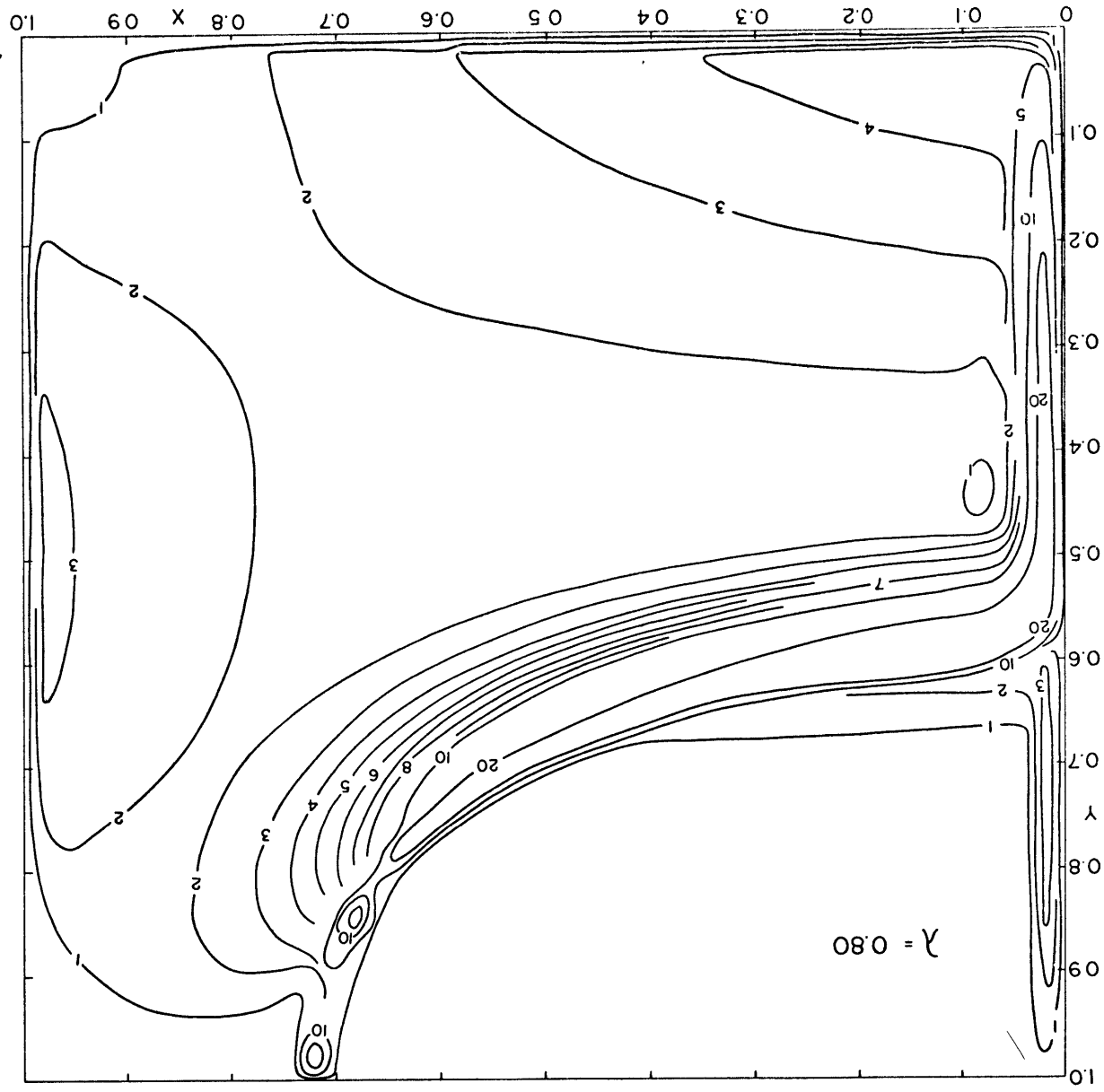Fig. 5c. Non-dimensional Surface Layer Depth ($\lambda = 0.80$)

Fig. 6a. Non-dimensional Surface Layer Speeds (λ = 0.40)

Fig. 6b. Non-dimensional Surface Layer Speeds (λ = 0.60)

λ = 0.60

39

Fig. 6c. Non-dimensional Surface Layer Speeds ($\lambda = 0.80$)

where it exists and the depth of the surfaced lower layer in the northwest corner of the basin. Fig. 6 gives the distribution of particle speeds; a, b, and c correspond to λ = 0.40, 0.60, and 0.80, respectively. The quantities in Figs. 4-6 are presented in non-dimensional units. To convert to dimensional form, multiply the displayed values in Fig. 4 by 1.75×10^{13} $cm^3 s^{-1}$, those in Fig. 5 by 3×10^4 cm and those in Fig. 6 by 0.9697 cm s^{-1}.

Examination of Figs. 4-6 shows that the circulation increases, the thermocline deepens and higher flow speeds result from increasing the wind stress parameter. The change in the lower layer is more dramatic due to the combined effects of stronger wind, greater area of water exposed to the wind and southward penetration into an area of greater wind stress curl.

Integration of the oceanic thermal equation is done by a Lagrangian technique. We follow individual parcels around streamlines calculating the temperature change from the vertical flux of heat into the parcel. We thus do not explicitly calculate the heat advection term. The major advantage of this method is that it places a large number of points in the boundary layers where the streamlines are close together.

In the upper layer, ten equally spaced streamlines are selected in the interval between the maximum value of the streamfunction and zero. Similarly, three equally spaced

streamlines are chosen in the lower layer. A search is conducted for crossings of individual streamlines with horizontal gridlines (grid crossings). Velocities and depths are interpolated onto these grid crossings. The distances between grid crossings along streamlines are calculated. The traversal times between grid crossings are then found using the velocities at the grid crossings and the distances between the crossings. We assume that the velocity at a given crossing holds along the streamline halfway to the upstream and downstream crossings. We then sum the traversal times around streamlines to arrive at the total traversal times for parcels of fluid around particular streamlines.

Each streamline is then divided into an equal number of segments with the property that on a given streamline the segment traversal time is uniform. The segment endpoints (streamline points) will be the points at which the thermo-dynamic equation will be integrated. This procedure makes the thermodynamic integration very direct. Fig. 7 schematically illustrates the above calculations. The cases presented in this paper were run with 200 integration points per streamline.

An atmospheric temperature distribution and an initial oceanic temperature distribution are specified. The temperatures at the streamline points are then stepped forward in time, the values at the end of a time step being equal to the
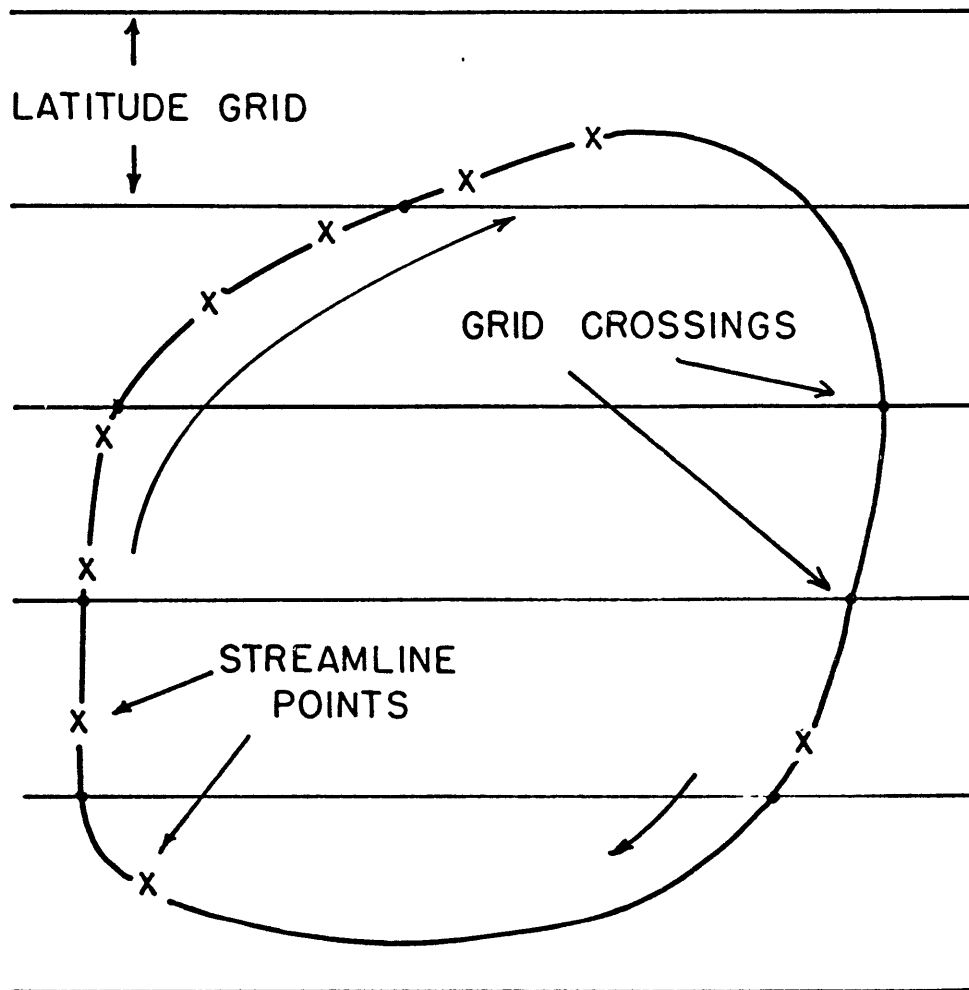
Fig. 7. Determination of Integration Points for Thermodynamic Equation

values at the upstream gridpoints after the previous time
step plus the heat added during the time step. This heat
addition, according to our linear law, is proportional to
the difference between the average atmospheric temperature
at the two points and the oceanic temperature at the
upstream point.

It is only meaningful to discuss equilibrium solutions
with this method. The time step varies with streamline
because we have taken the same number of points along every
streamline and the total traversal time varies with stream-
line. Therefore, since the temperature field on each stream-
line is evolving in its own time frame, the overall tempera-
ture field after an arbitrary amount of integration time is,
in general, unknown.

Testing for convergence of the ocean temperature
integration is handled in the following fashion. Equili-
bration occurs because of the damping nature of the forcing.
The effect of the heat flow term is to diminish temperature
differences between the atmosphere and the ocean. Areas
of rapid currents in which parcels travel great distances
during the thermal forcing decay time are the only regions
in which significant differences between the oceanic and
atmospheric temperatures occur.

When the process is simulated in finite difference
form the major problem we encountered was an oscillatory
instability. If the temperature of a given parcel was

sufficiently far from the atmospheric temperature and the
time step was large enough, the parcel would greatly over-
shoot the equilibrium point.

This problem was solved by decreasing the time steps
of integration by increasing the number of points around
the streamlines so that unrealistically large forcings for
long periods of time were not present and oscillatory
damping or simple damping was realized.

At each integration point on a given streamline for each
time step we compared the ΔT_0 of the parcel during the time
step as it moved form the upstream gridpoint to the same ΔT_0
from the previous time step. If for all streamline points
the absolute value of the change in the ΔT_0's from the
previous time step was less than a threshold value the
streamline was said to have converged and integration was
discontinued on that particular streamline. Table 2 depicts
for a standard case the number of time steps and the total
time for equilibration for each of the streamlines used in
the integration as a function of the convergence threshold
value. For the cases we have run the tolerance was set to
10^{-8}°C, the minimum resolvable by our single precision
calculation.

Given the equilibrium distribution of oceanic temperature
it is possible to calculate a number of quantities. The
first thing that we looked for was the northward flux of heat
in the surface layer across a latitude wall in the basin.

TABLE 2

λ = 0.45 C_{HF} = 8000 cal cm^{-2} yr^{-1} °C^{-1}

ATMOSPHERIC TEMPERATURE DIFFERENCE
BETWEEN N-S WALLS = 24 °C

INTEGRATION TIME FOR CONVERGENCE IN YEARS
NUMBER OF TIME STEPS FOR CONVERGENCE

NON-DIMENSIONAL STREAMLINE VALUE

CONVERGENCE THRESHOLD	0.1	0.2	0.3	0.4	0.5	0.6	0.7	0.8	0.9	1.0	0.04	0.08	0.12
1. x 10^{-1}	1.8	1.2	0.5	0.2	0.2	0.1	0.1	0.1	0.1	0.1	1.1	0.7	0.6
	14	11	5	2	2	2	2	2	2	2	2	2	2
1. x 10^{-2}	5.2	4.8	4.2	3.7	3.3	2.8	2.2	1.7	1.0	0.8	16.1	9.1	5.0
	40	45	45	45	43	41	36	31	20	2	29	25	18
1. x 10^{-3}	8.4	7.7	7.3	7.0	6.7	6.4	6.0	5.7	5.3	4.6	32.7	26.3	22.3
	64	73	79	84	88	94	98	102	107	111	59	72	80
1. x 10^{-4}	11.0	10.4	10.1	9.9	9.8	9.9	9.9	9.9	9.7	9.2	49.9	43.4	39.5
	84	98	109	120	130	146	161	175	196	220	90	119	142
1. x 10^{-5}	13.8	13.1	13.3	13.3	13.8	13.9	14.3	14.4	14.3	14.1	67.1	60.9	56.7
	106	123	143	161	182	204	233	255	291	337	121	167	204
1. x 10^{-6}	16.9	20.1	21.6	20.0	20.1	23.3	23.4	22.5	21.2	21.8	84.3	78.8	74.5
	130	189	233	241	265	342	381	399	430	521	152	216	268
1. x 10^{-7}	19.3	21.9	23.1	25.7	23.6	26.6	31.6	29.1	31.1	34.5	117.	109.	110.
	148	206	249	310	312	391	515	517	632	823	211	298	394
1. x 10^{-8}	19.3	21.9	23.1	26.0	23.7	26.6	31.6	29.1	31.1	34.5	134.	144.	129.
	148	206	249	314	313	391	515	517	632	823	241	396	462

This was done by interpolating the equilibrium temperature from the streamline points back onto the grid crossings. Latitude lines were then broken up into segments on which the northward speed, mixed layer depth and oceanic temperature were taken to be that of the grid crossing within the segment. After eliminating slight net mass flows across latitude lines and subtracting the zonally averaged values of temperature, these quantities were then summed across the width of the basin, appropriately weighted by segment length. This calculation requires special treatment of latitude lines which intersect the line of separation.

It was decided to numerically analyze and contour the large number of maps desired. The contouring routine required values on a regular grid of points. Therefore, we needed to objectively analyze our solution for the oceanic temperature at the streamline points onto our original square grid. Since we had at our disposal a potentially infinite number of data points, the particular objective analysis scheme chosen was not crucial.

A Cressman-type analysis scheme was chosen. This scheme consists of an initial guess field which is corrected using the data during a sequence of scans. The difference between the data and a bilinear interpolation from the four corners of the grid box containing the data point is computed for all gridpoints. These anomalies are used to correct the analyzed field at all gridpoints within a specified scan

radius of the data point. The scanned area is elliptical in shape with an east-west major axis to better resolve zonally coherent patterns and the weight given a correction from a given data point decays with distance from the data point. We simplified Cressman's scheme by eliminating data quality checks and initial smoothing operations.

The adjustable parameters (weights, scan radius, eccentricity) for the analysis scheme were varied until the routine gave the best agreement with hand analyzed maps. Because of the extremely large number of data points (2600 in the results presented) in our 6000 km square grid, changes in the analysis parameters caused only extremely subtle changes in the results. Tracings were made of the computer maps to give the displayed results.

Use was made of our analyzed oceanic temperatures along with the specified atmospheric temperatures, which were analytic functions of x and y and could be easily evaluated at gridpoints and streamline points, to give the vertical heat flux into the ocean in the final state from the linear heat flux law.

IV. Experiments

Equilibrium thermal states of the model ocean were
calculated subject to a variety of fixed atmospheric config-
urations. Three distributions of atmospheric temperature
were chosen. They are all zonally uniform with uniform
meridional temperature gradients. The atmospheric temper-
atures at the southern walls of the basin are fixed at
30°C; the temperatures at the Northern wall are 12°C, 6°C,
and 0°C, respectively. We will call these the weak, medium
and strong gradient cases; the gradients are representative
of those over the North Atlantic for summer, annual average
and winter conditions (Figs. 8 a-c).

Results will be presented for the eleven different case
outlined in Table 3. The first case is a control run.
Following the control run are results which show the model
response to differing heat flux constants, wind stress
magnitudes and atmospheric temperatures. Then we present
results from two composite cases in which the forcings are
intended to simulate perpetual summer and winter conditions.
The last two cases show some behavior of the model with
significantly different values of C_{HF}.

The wind stress parameter was varied over a range
$(0.40 \leq \lambda \leq 0.80)$ which included Parsons' value (λ = 0.45)
and was wide enough to give a good visual dipiction of
model sensitivity. Haney (1971, 1974) and Takano (1975) have
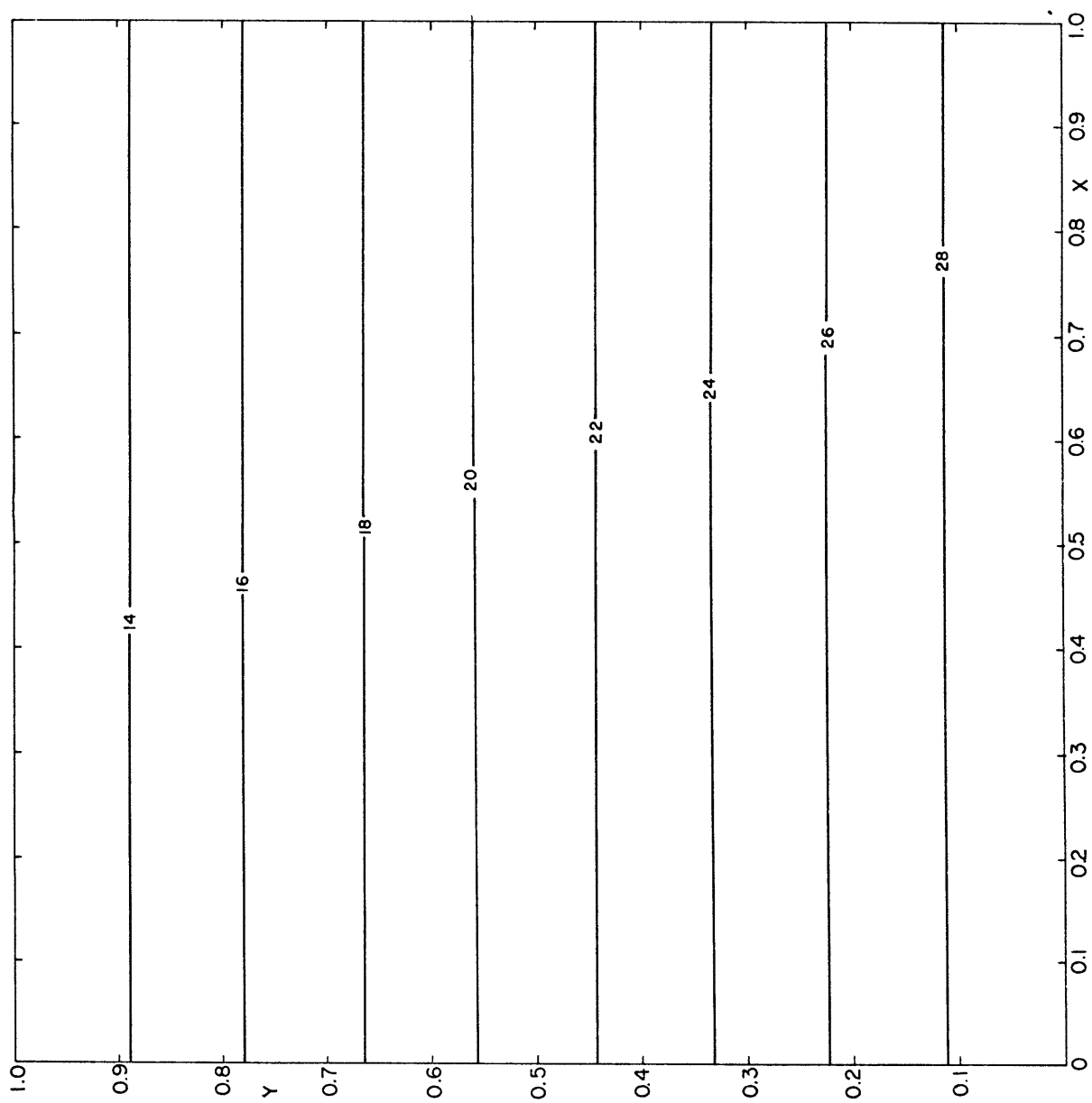
Fig. 8a. Atmospheric Temperature in °C ($\Delta T_A = 18°C$)
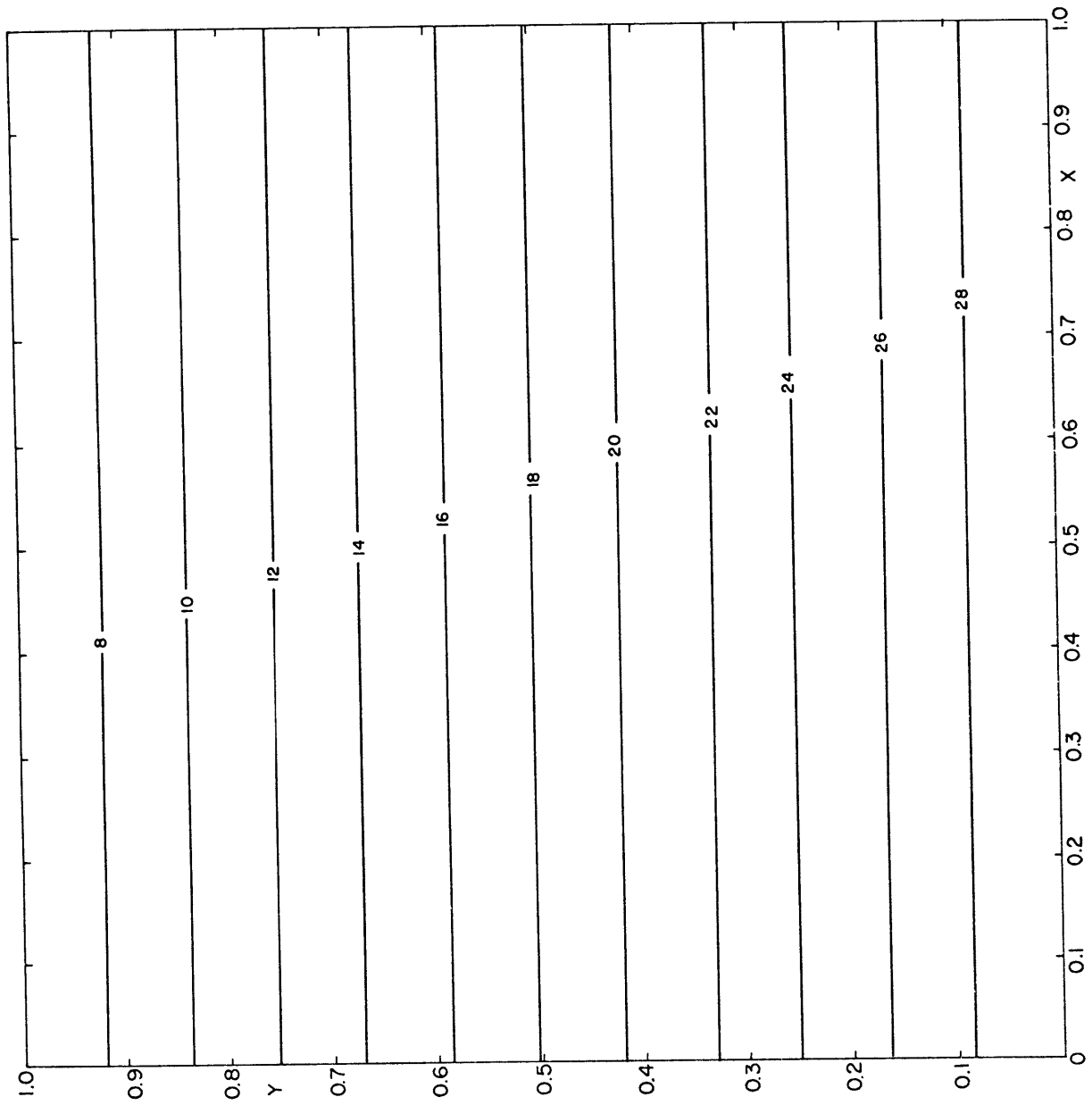
Fig. 8b. Atmospheric Temperature in °C ($\Delta T_A = 24$°C)
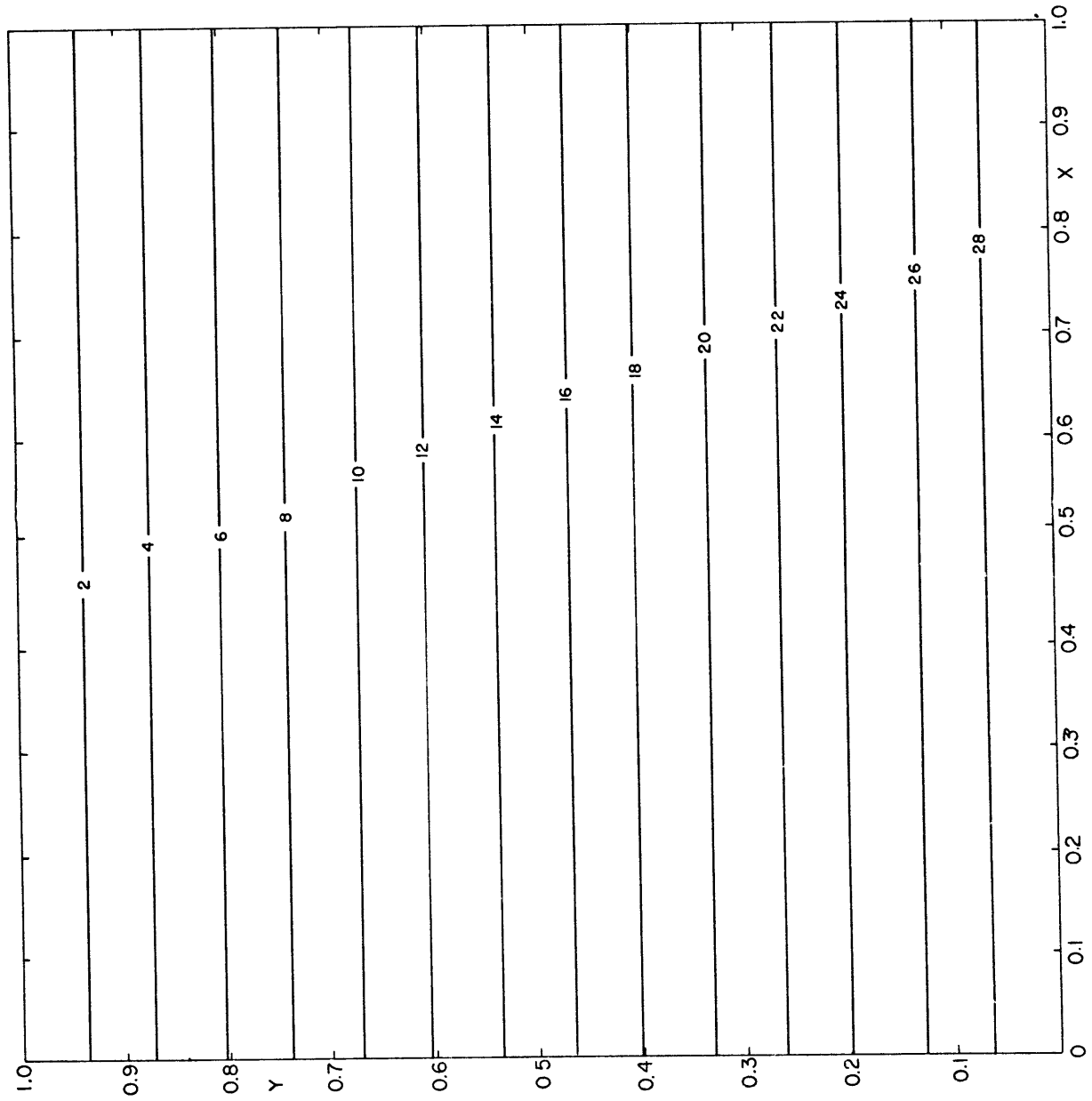
Fig. 8c. Atmospheric Temperature in °C (ΔT_A = 30°C)

TABLE 3

Case	λ	C_{HF} (cal cm^{-2} yr^{-1} $^\circ$C^{-1})	ΔT_A ($^\circ$C)
1	0.60	6000	24
2	0.60	8000	24
3	0.60	4000	24
4	0.80	6000	24
5	0.40	6000	24
6	0.60	6000	18
7	0.60	6000	30
8	0.40	4000	18
9	0.80	8000	30
10	0.60	2000	24
11	0.60	20000	24
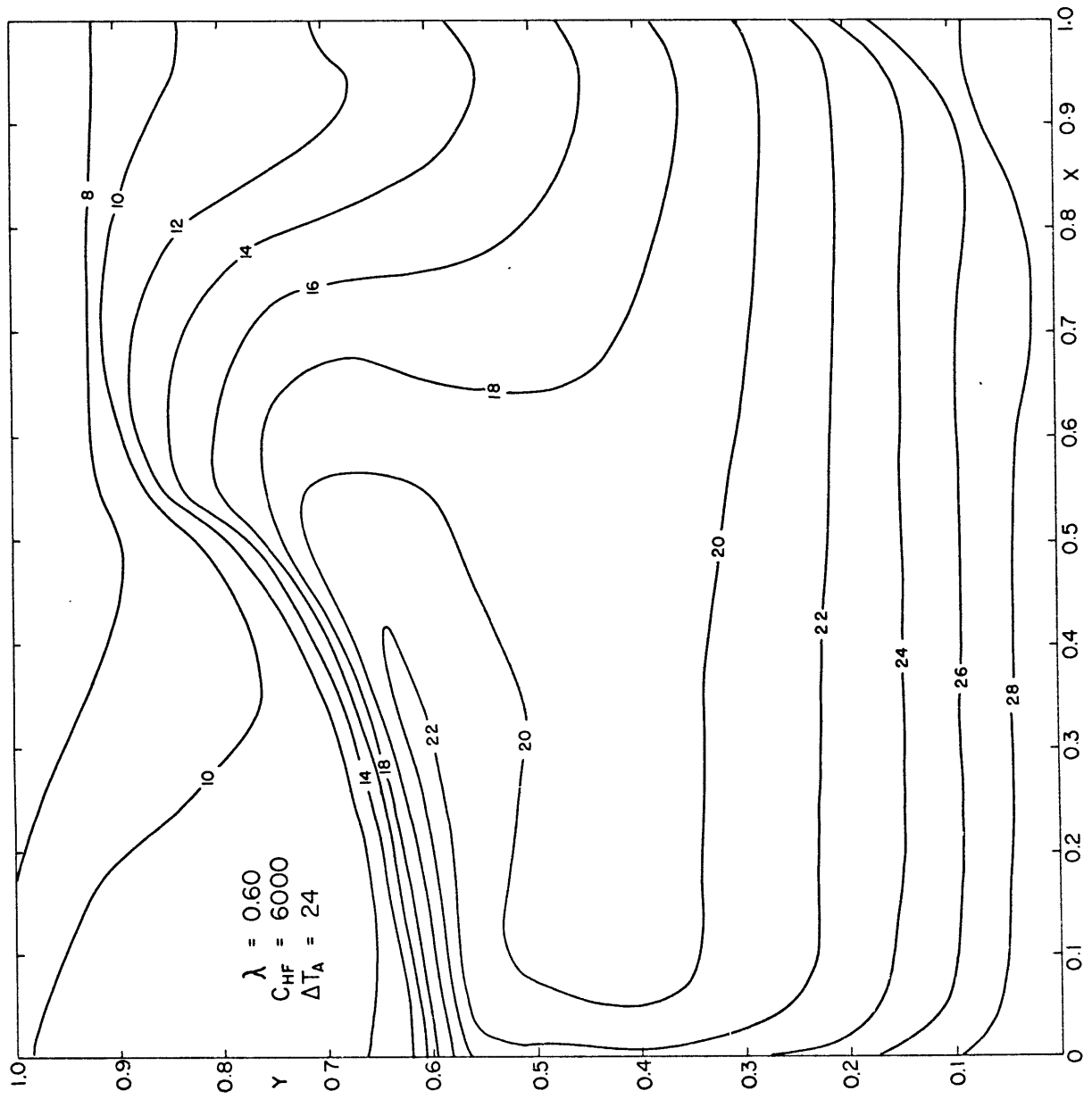
Fig. 9a. Equilibrium Oceanic Temperature in °C (Case 1)
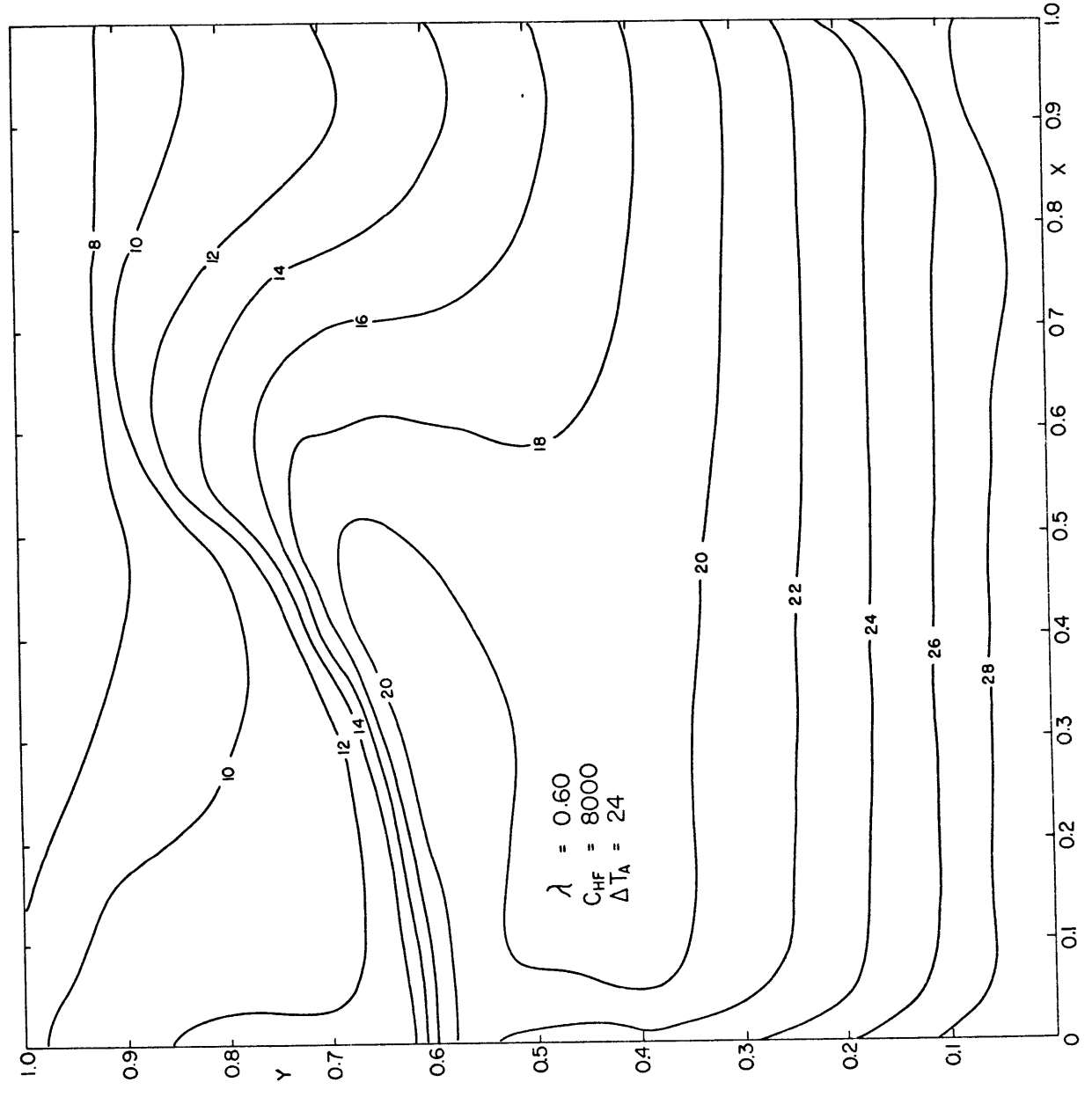
Fig. 9b. Equilibrium Oceanic Temperature in °C (Case 2)
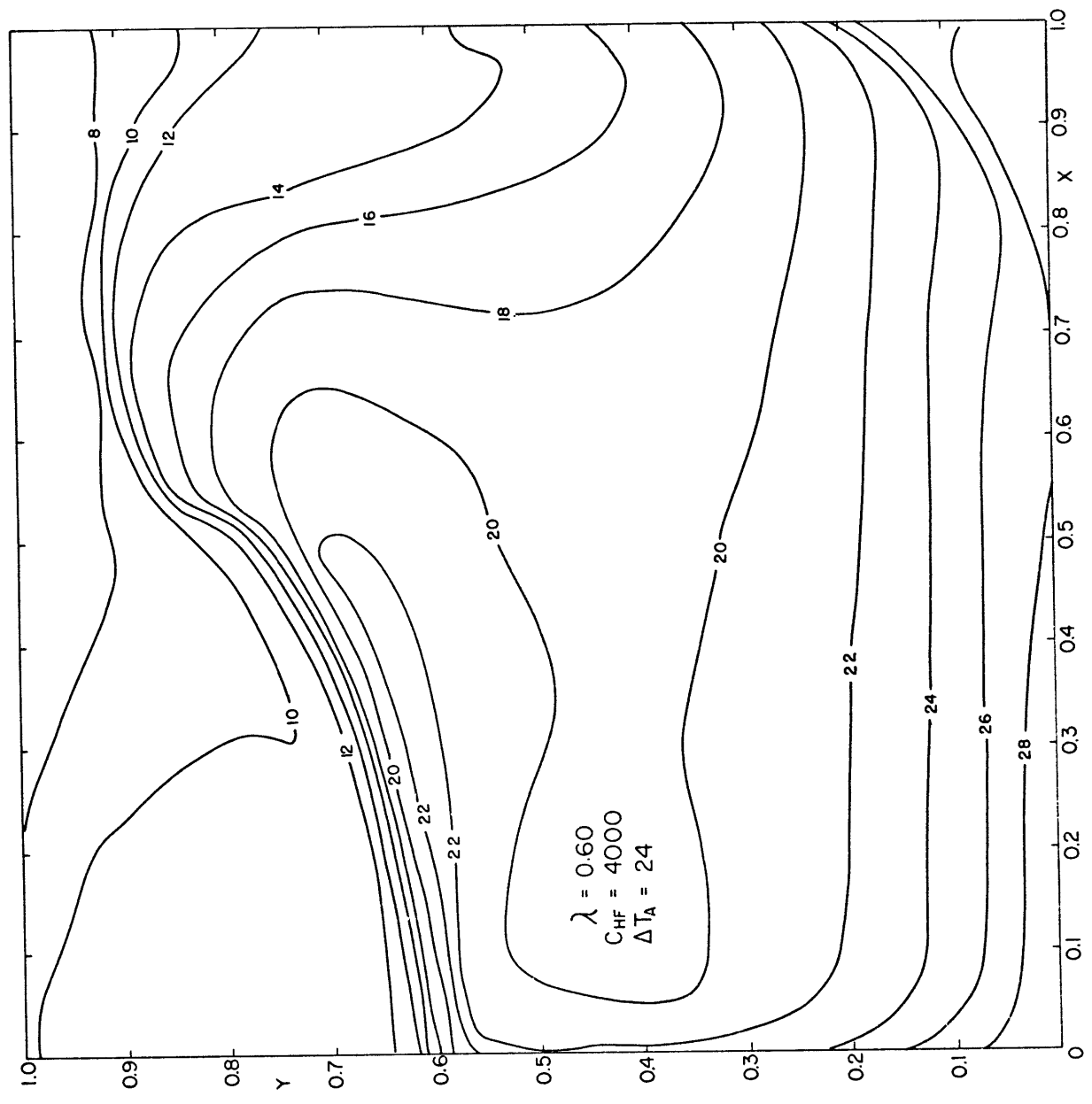
Fig. 9c. Equilibrium Oceanic Temperature in °C (Case 3)
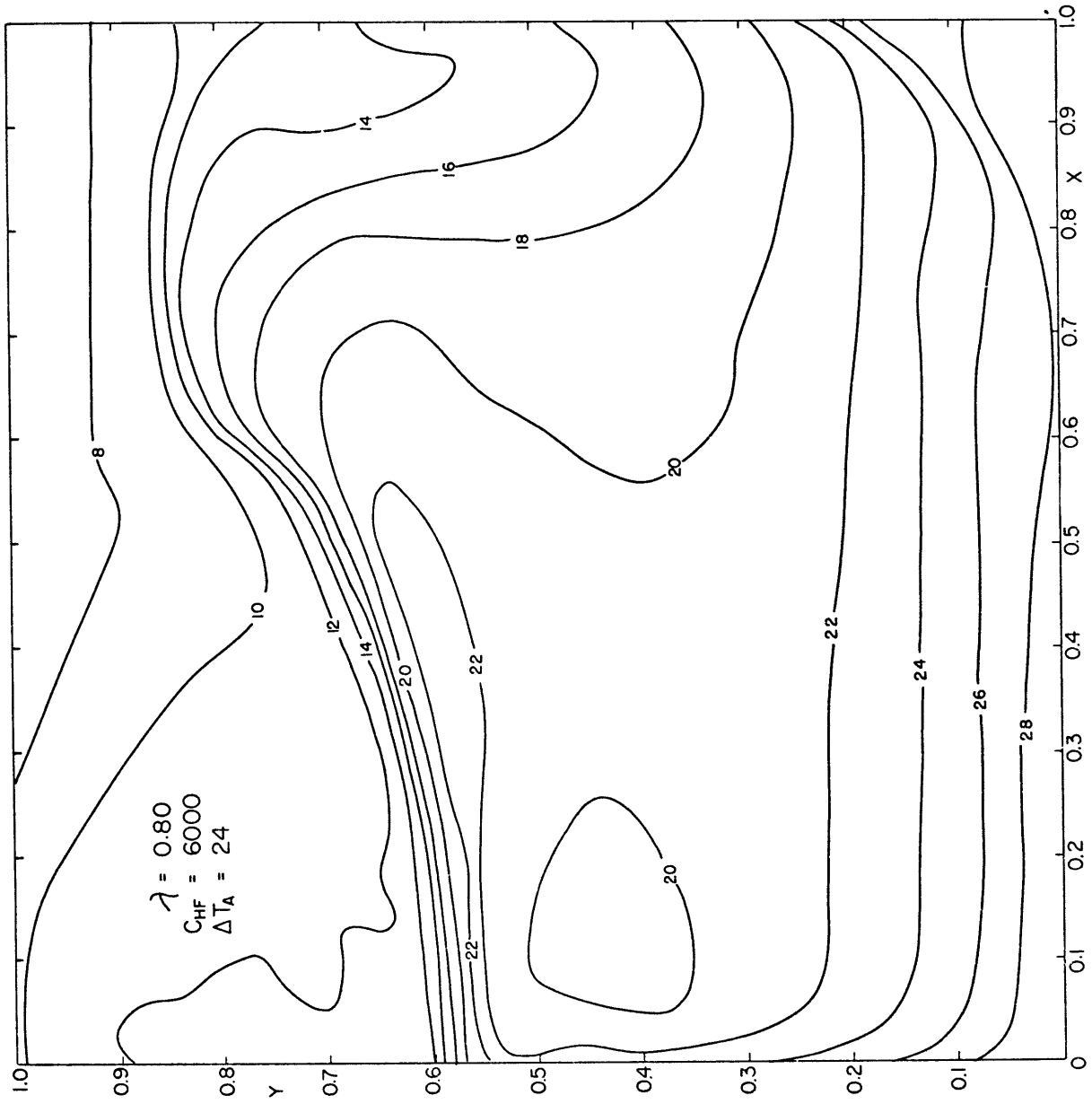
Fig. 9d. Equilibrium Oceanic Temperature in °C (Case 4)
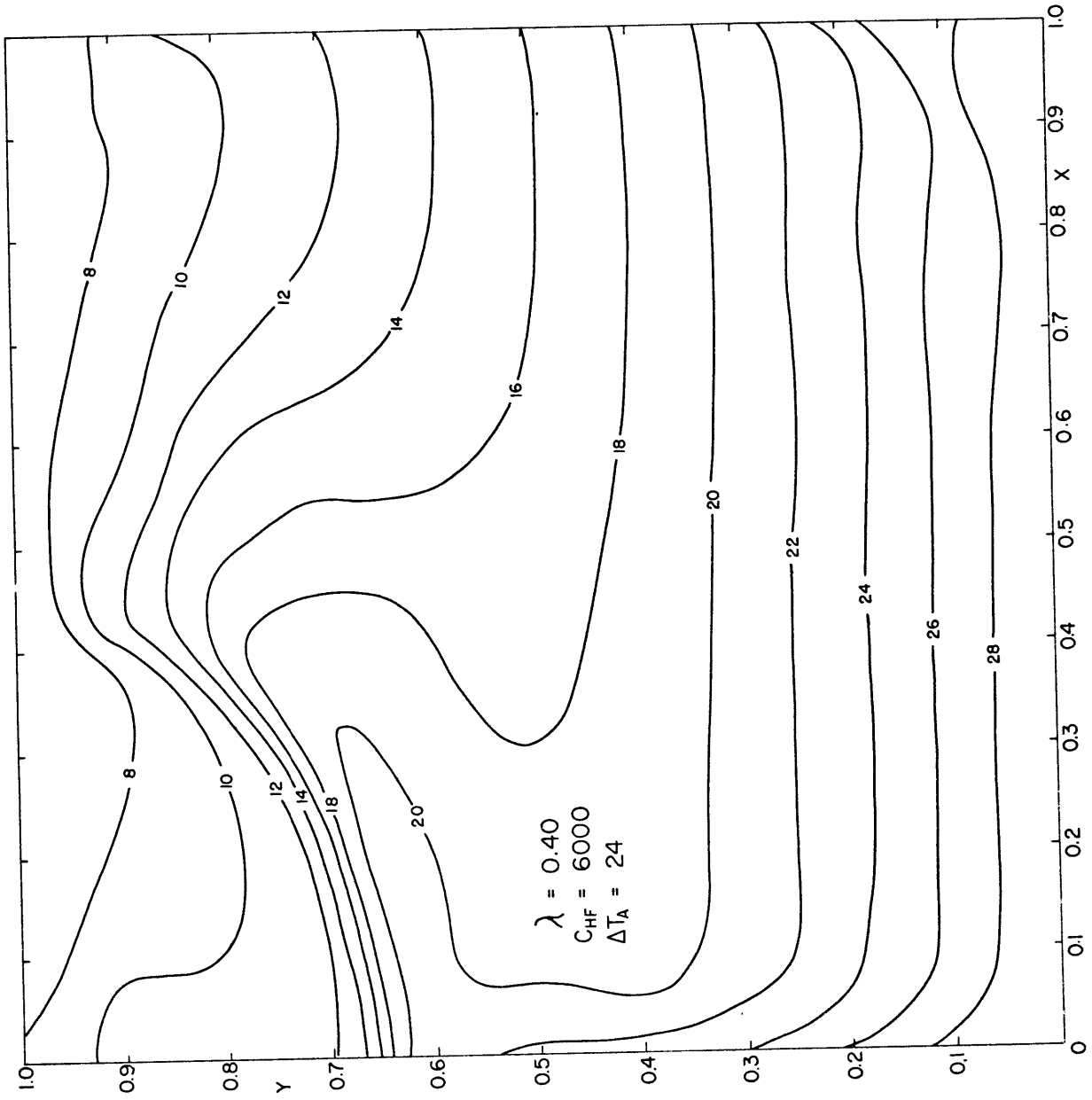
Fig. 9e. Equilibrium Oceanic Temperature in °C (Case 5)
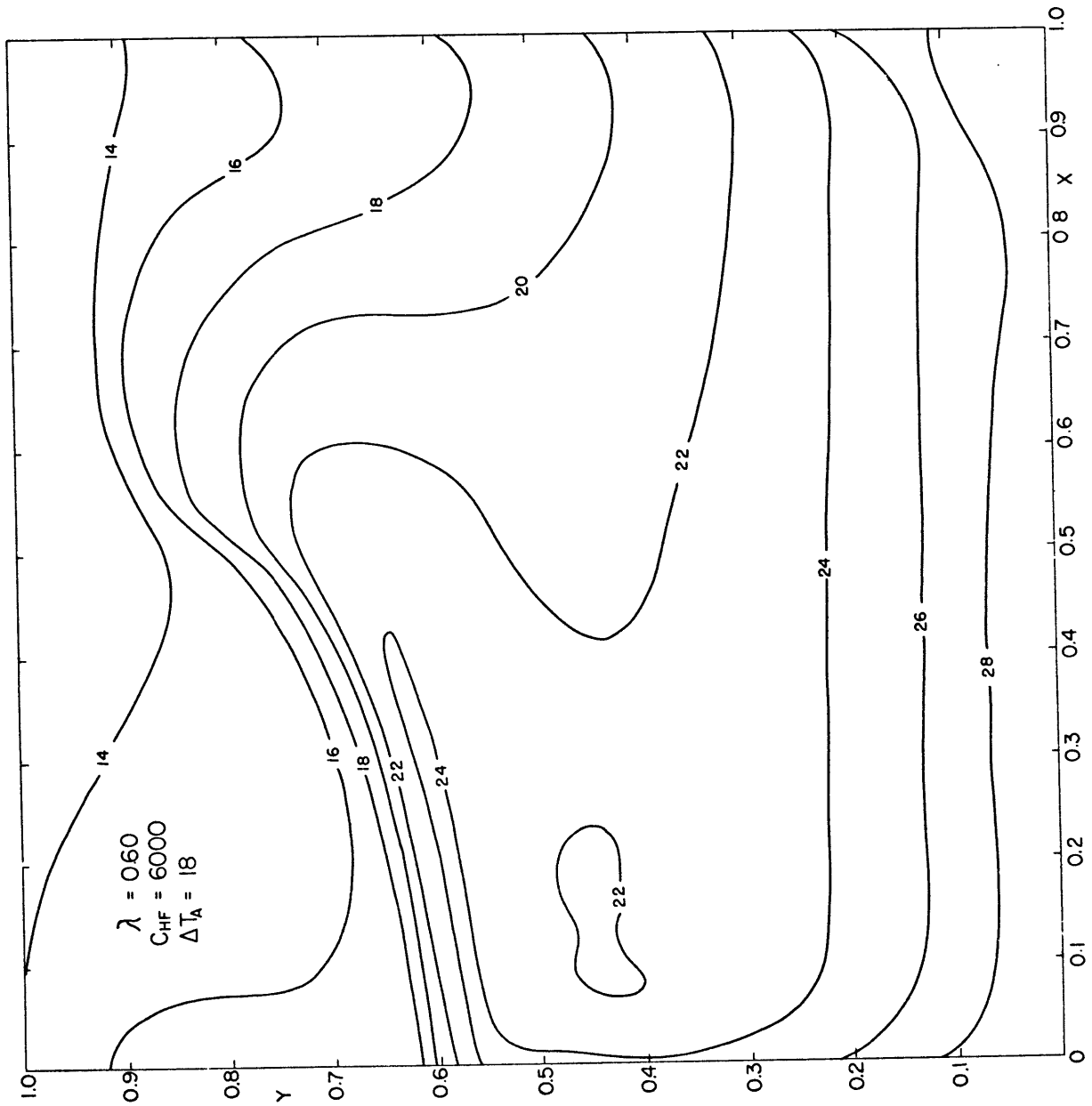
Fig. 9f. Equilibrium Oceanic Temperature in °C (Case 6)
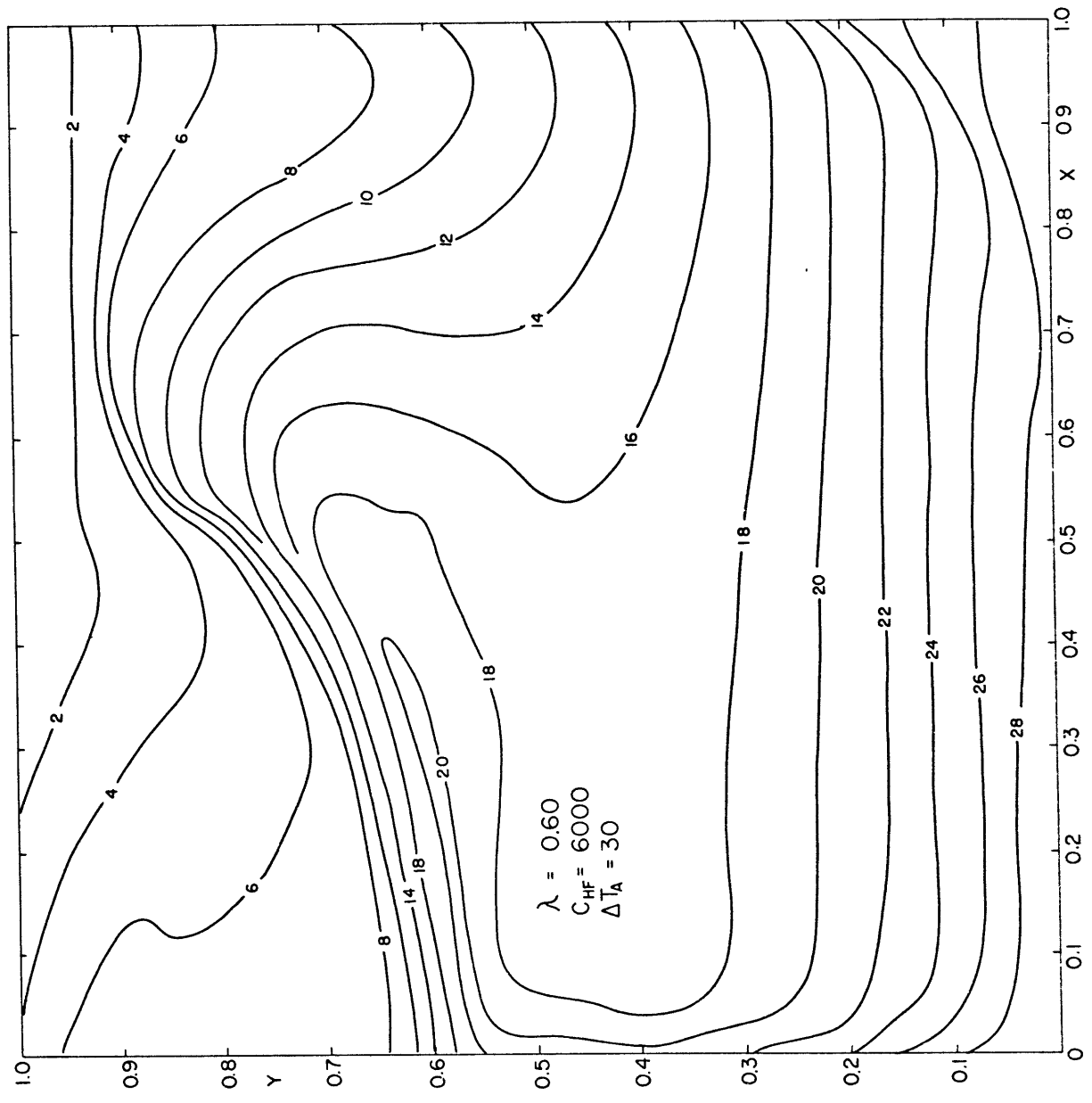
Fig. 9g. Equilibrium Oceanic Temperature in °C (Case 7)
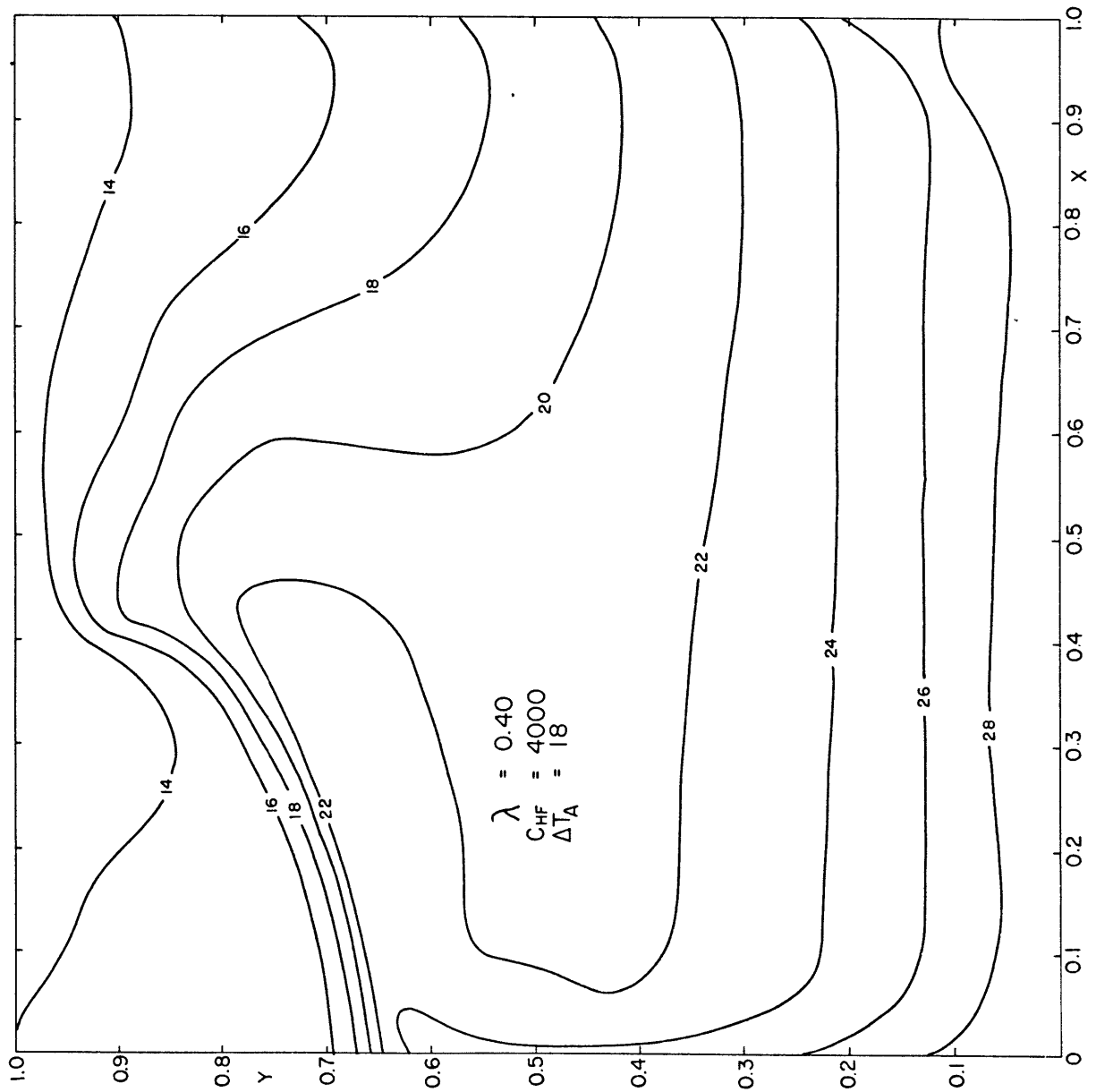
Fig. 9h. Equilibrium Oceanic Temperature in °C (Case 8)
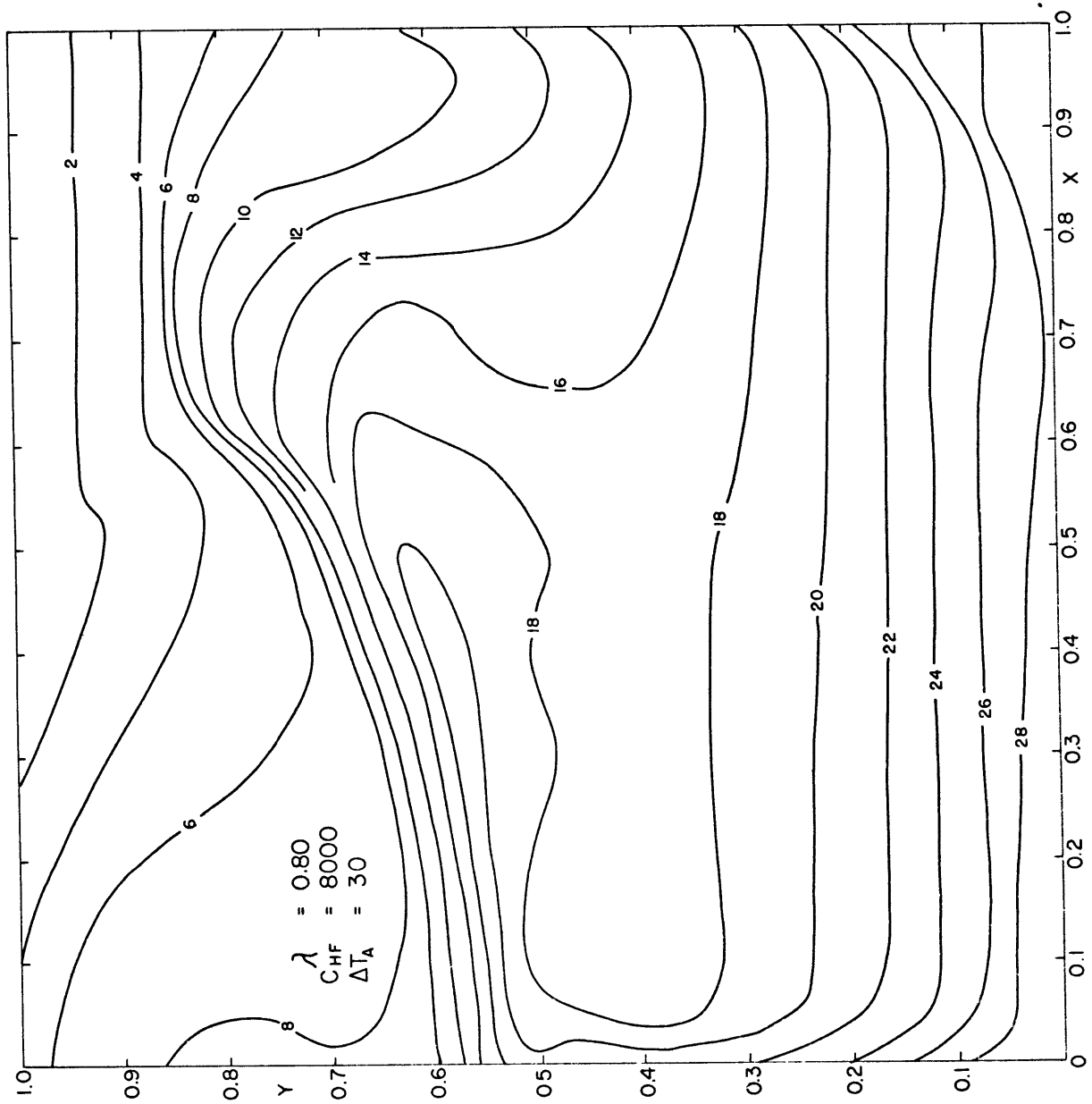
Fig. 9i. Equilibrium Oceanic Temperature in °C (Case 9)

63
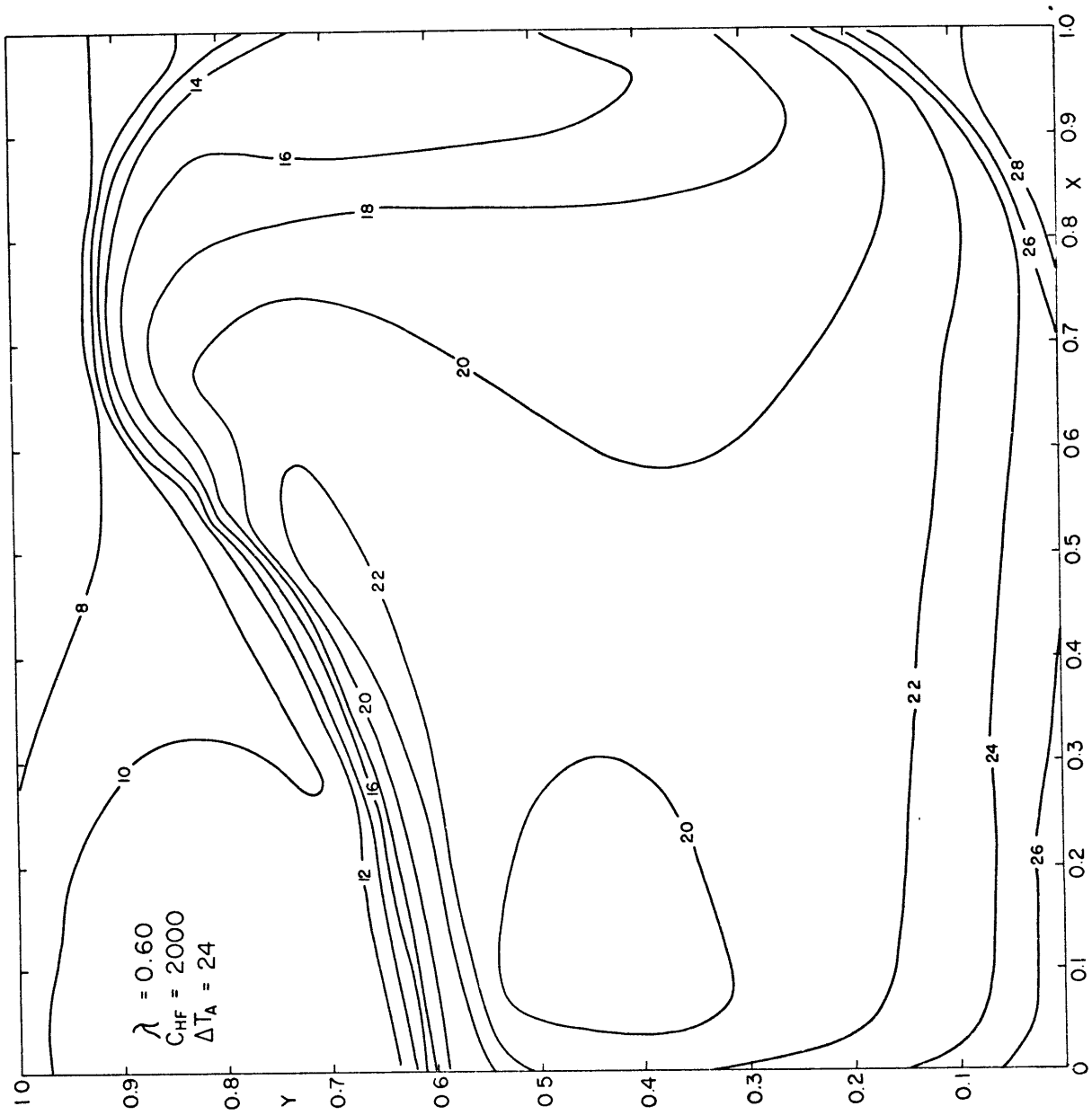
Fig. 9j. Equilibrium Oceanic Temperature in °C (Case 10)
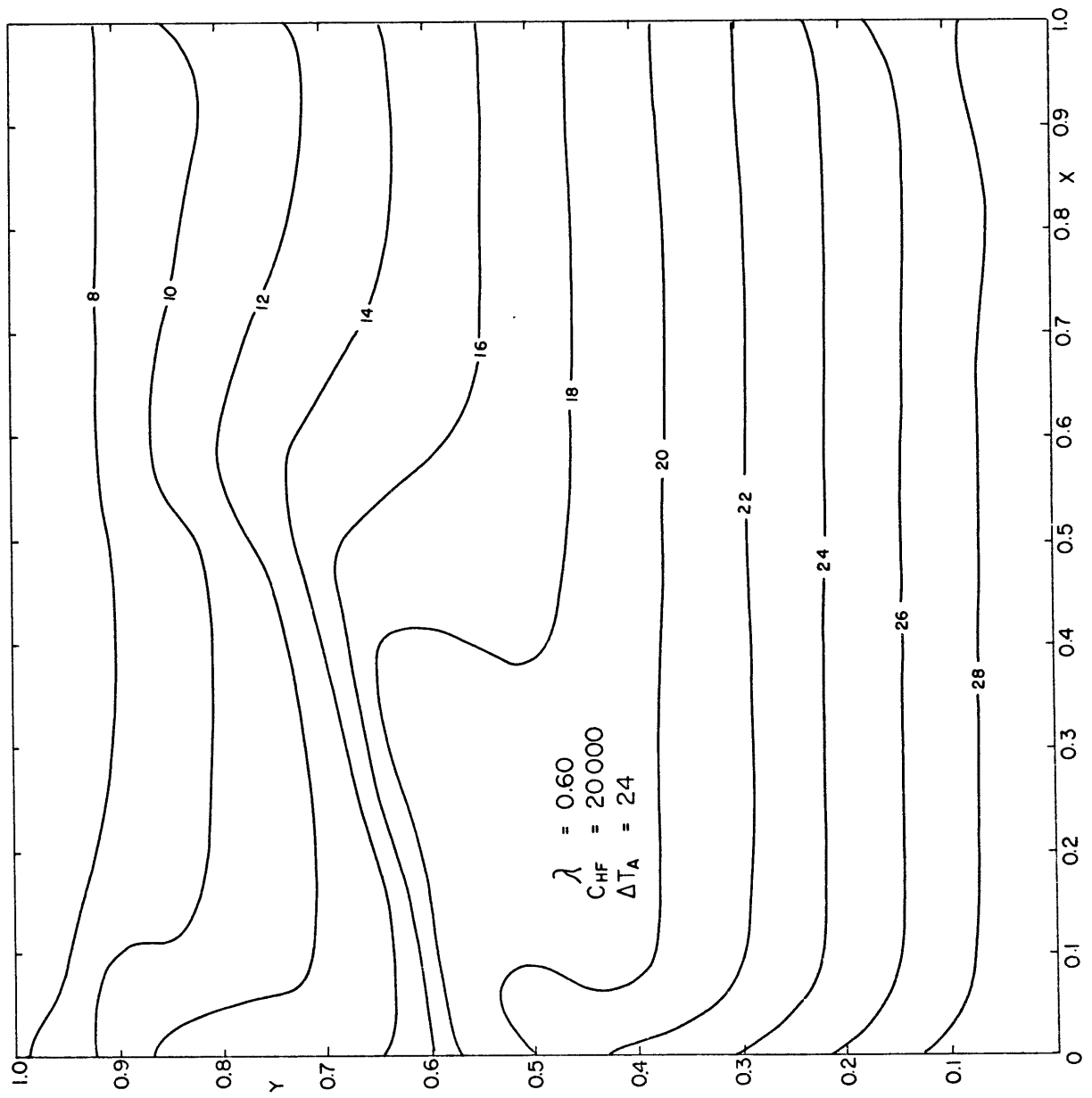
Fig. 9k. Equilibrium Oceanic Temperature in °C (Case 11)
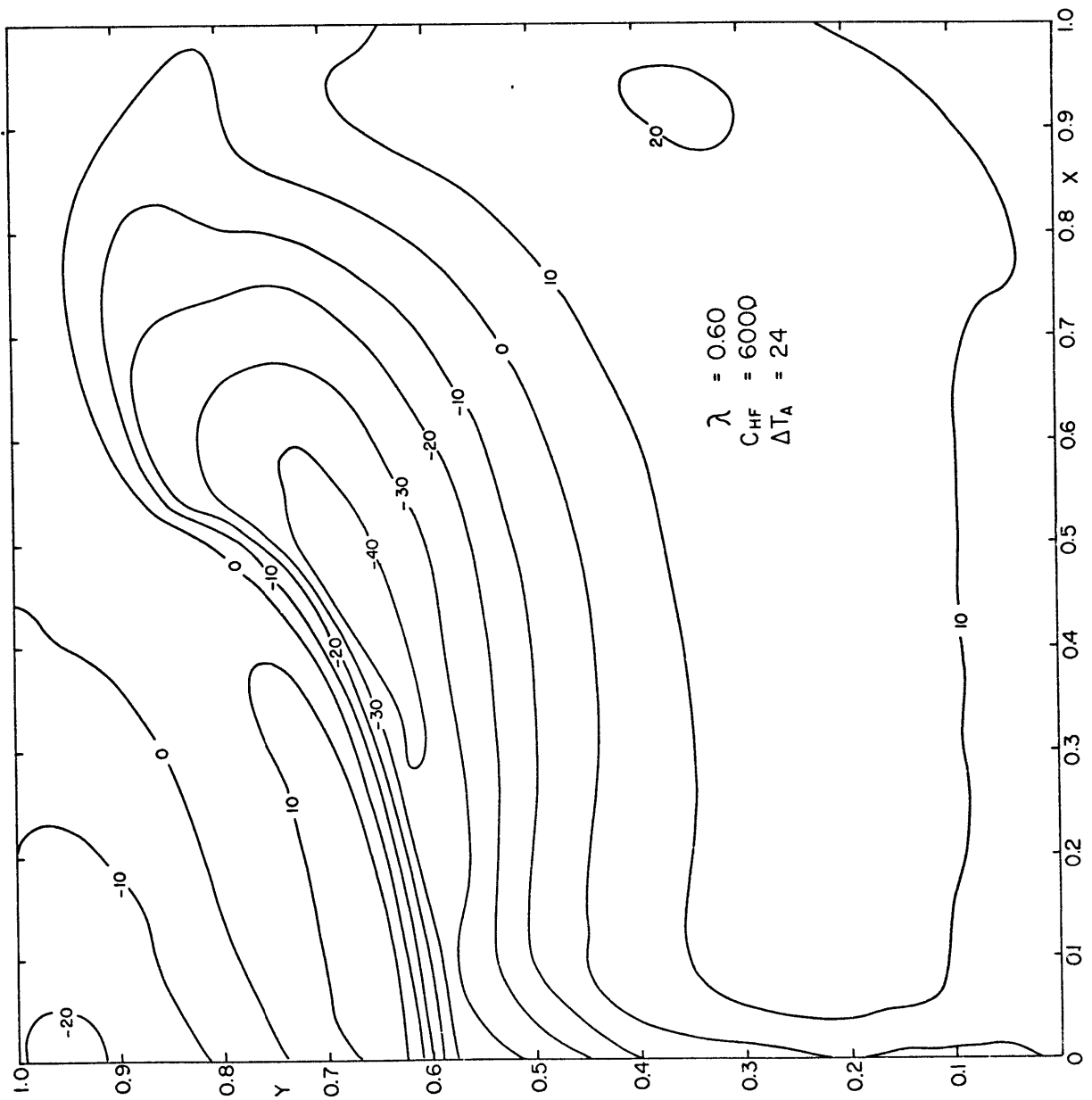
Fig. 11a. Equilibrium Vertical Heat Flux in kcal cm-2 yr-1 (Case 1)
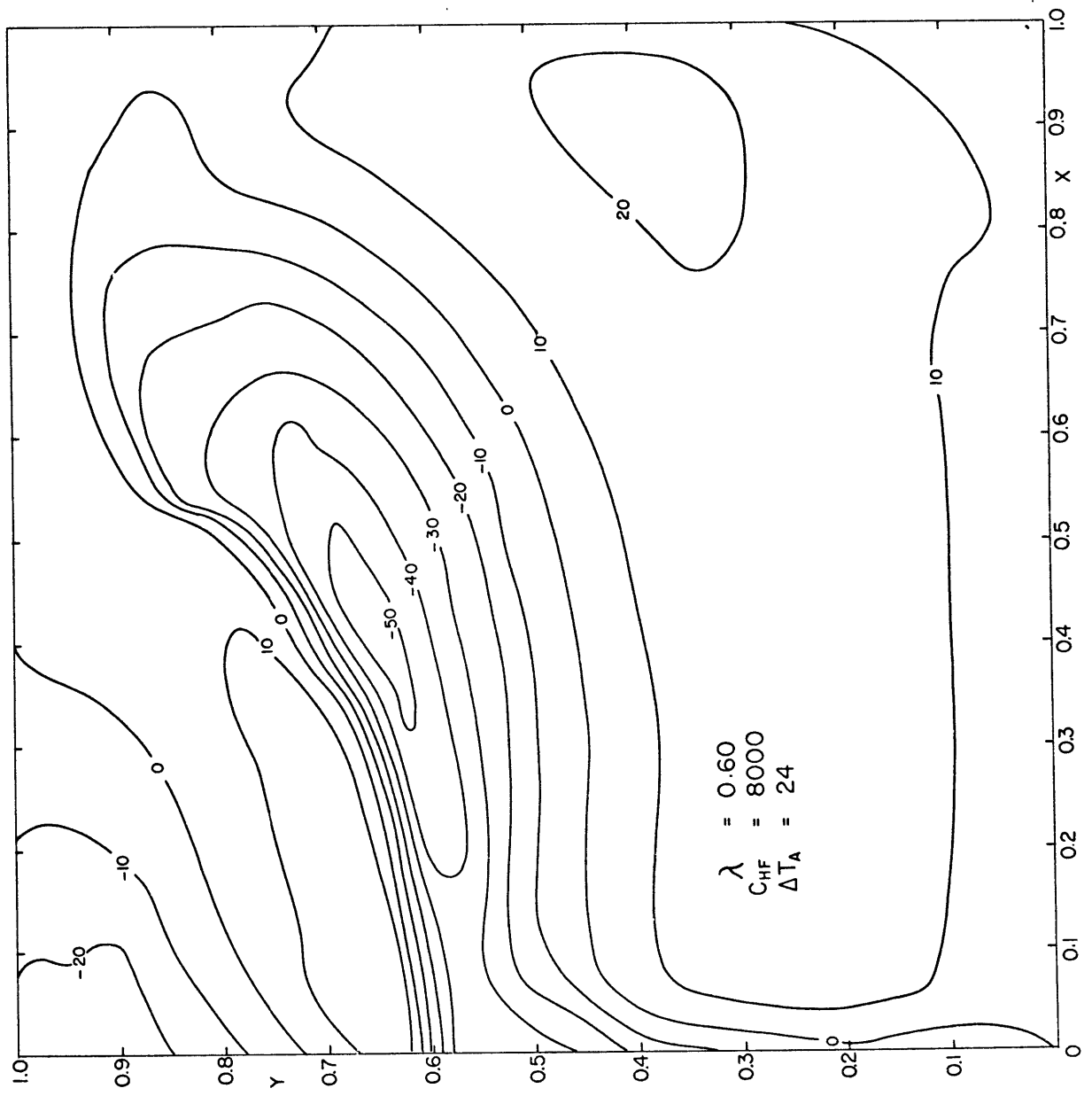
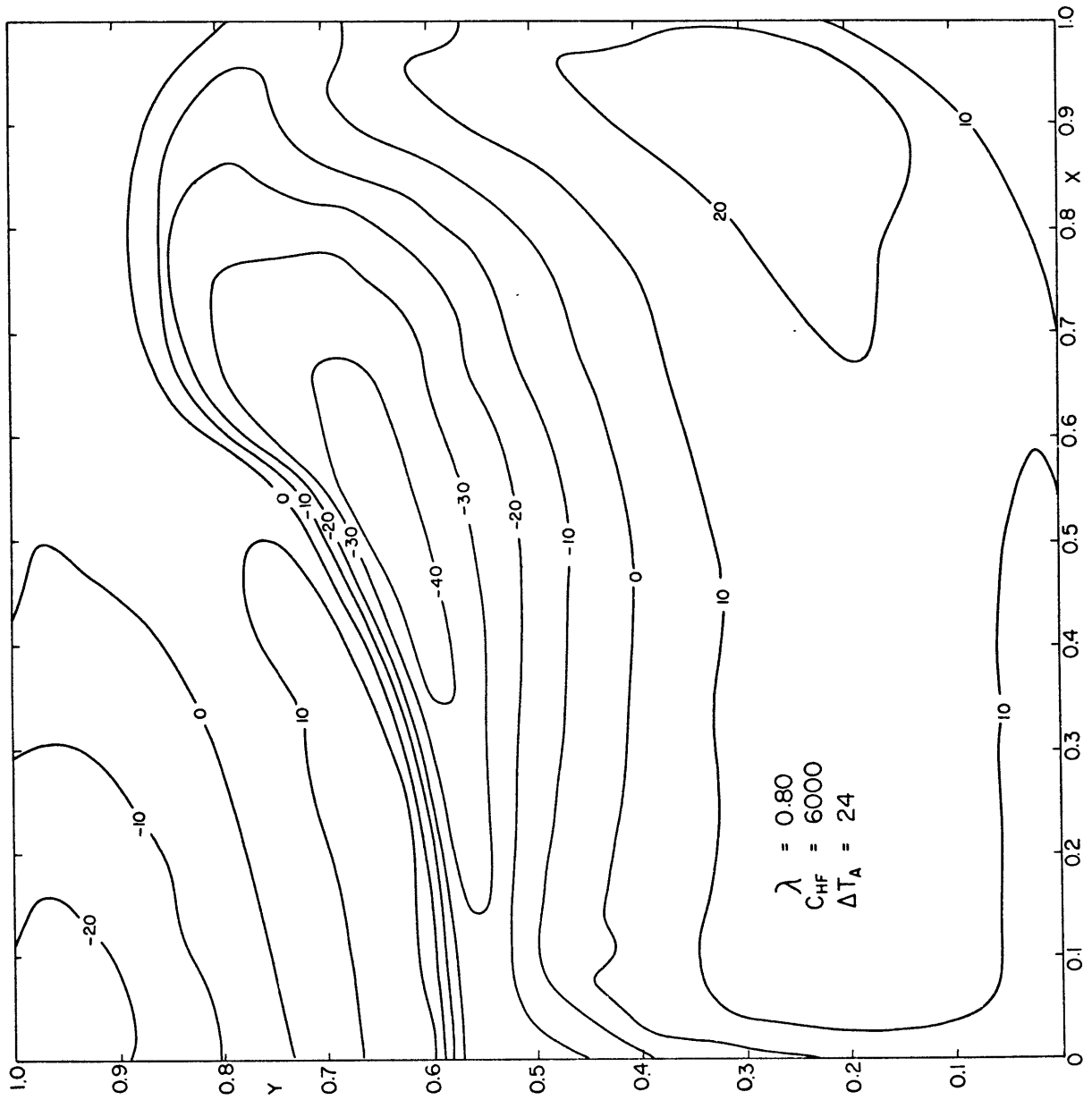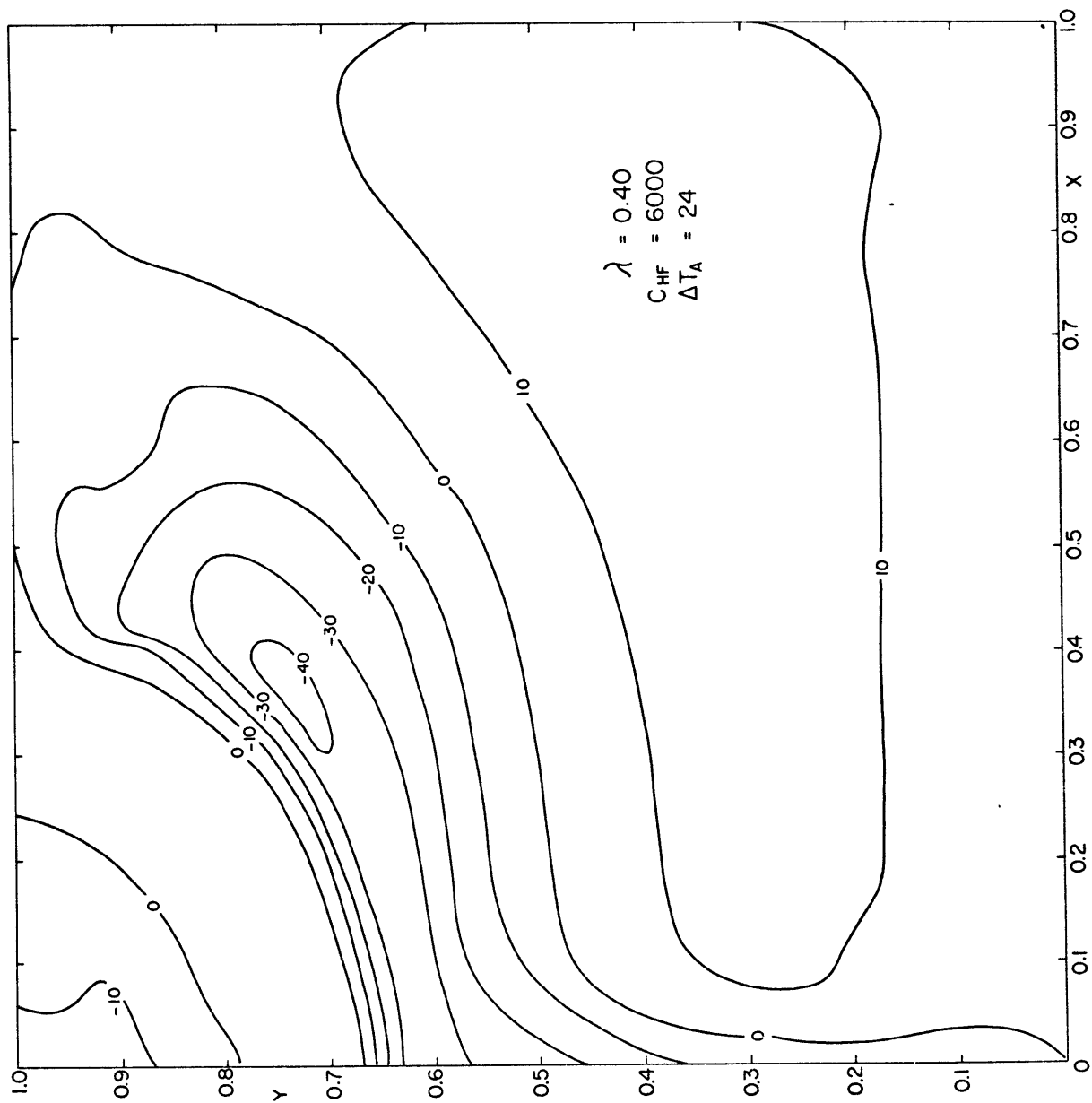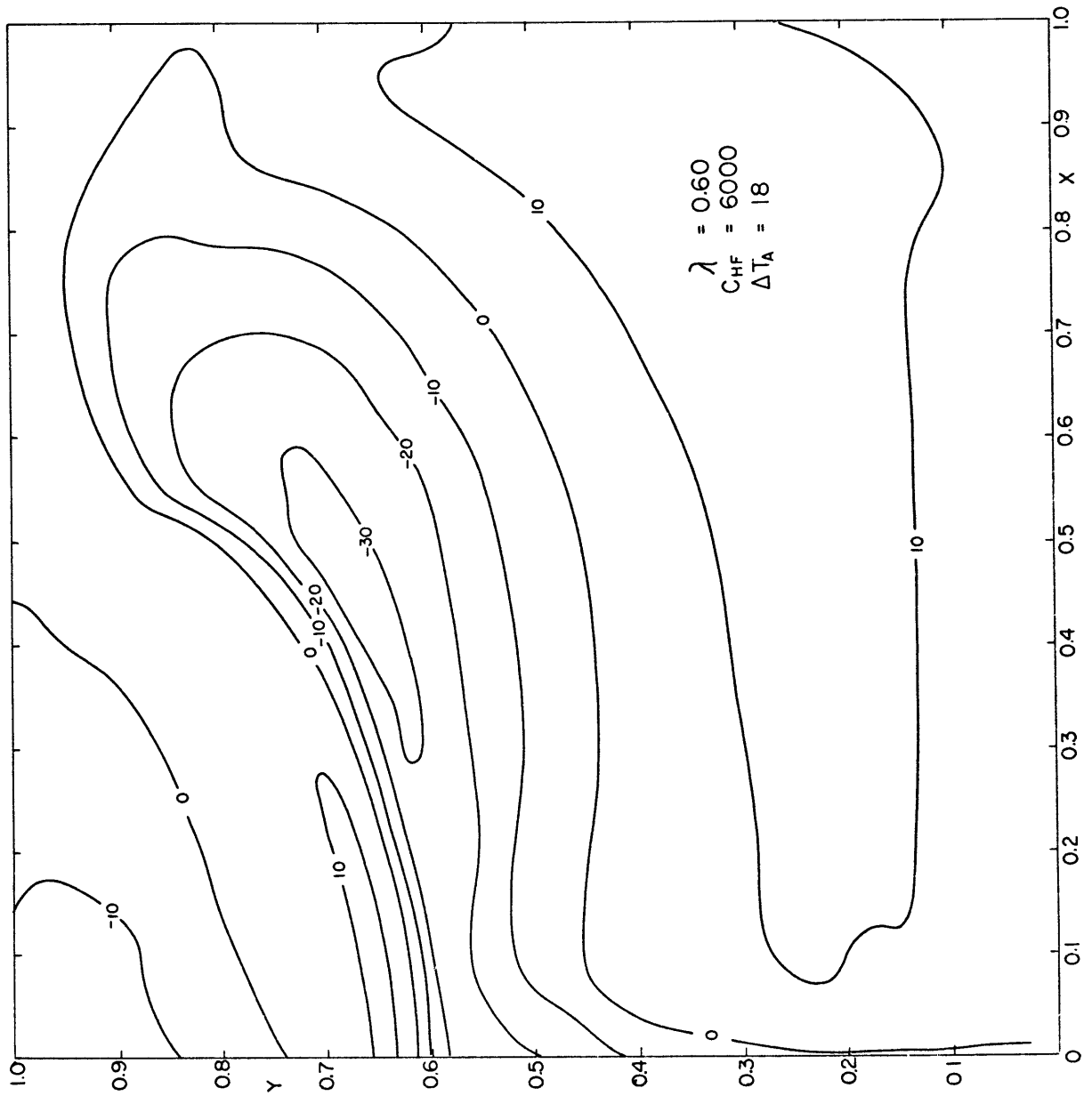**Fig. 11b.** Equilibrium Vertical Heat Flux in kcal cm-2 yr-1 (Case 2)
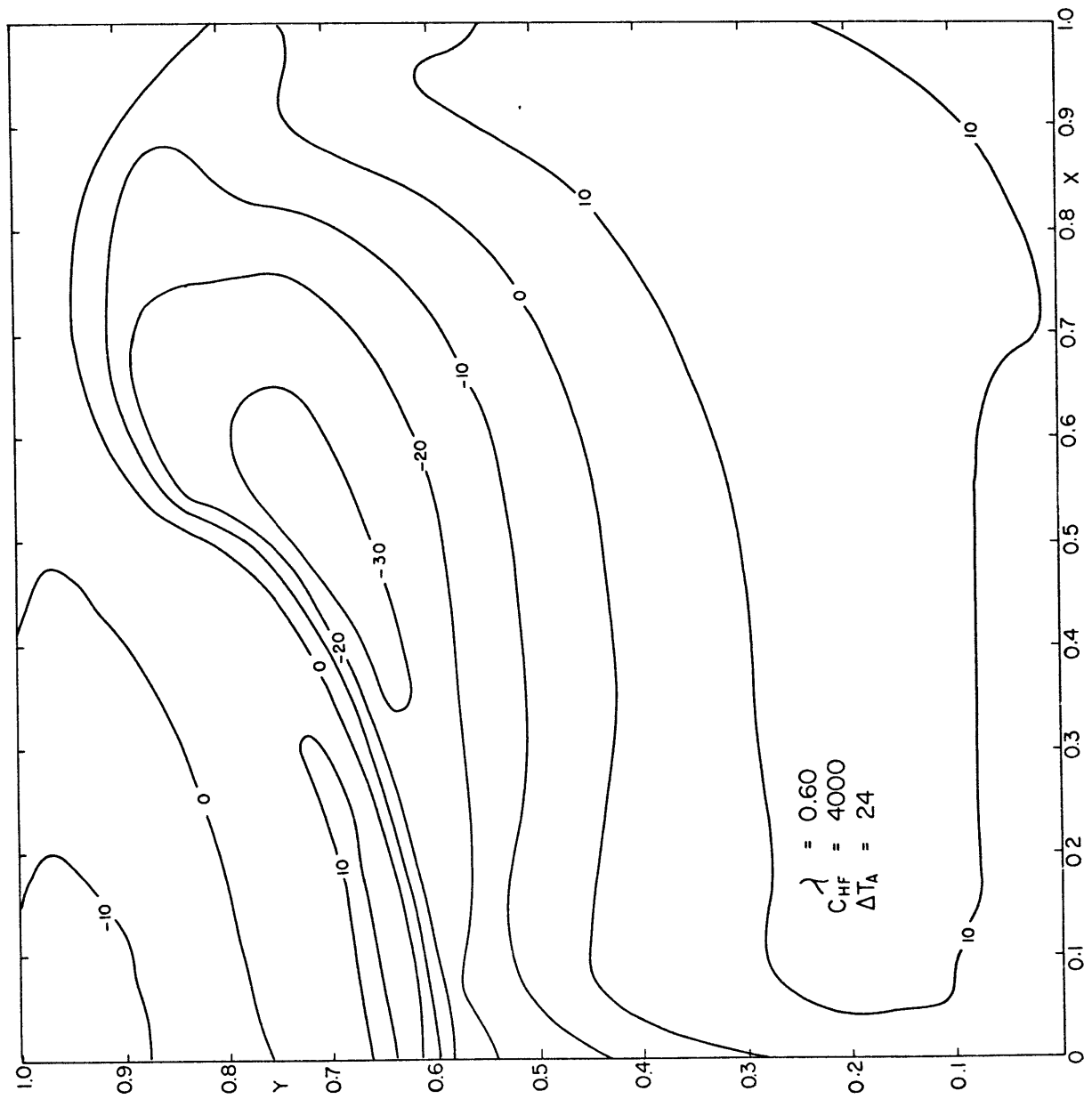
Fig. 11c. Equilibrium Vertical Heat Flux in kcal cm^{-2} yr^{-1} (Case 3)

68

Fig. 11d. Equilibrium Vertical Heat Flux in kcal cm^{-2} yr^{-1}
(Case 4)

Fig. 11e. Equilibrium Vertical Heat Flux in kcal cm^{-2} yr^{-1} (Case 5)

λ = 0.60
C_{HF} = 6000
ΔT_A = 18

Fig. 11f. Equilibrium Vertical Heat Flux in kcal cm^{-2} yr^{-1}
(Case 6)

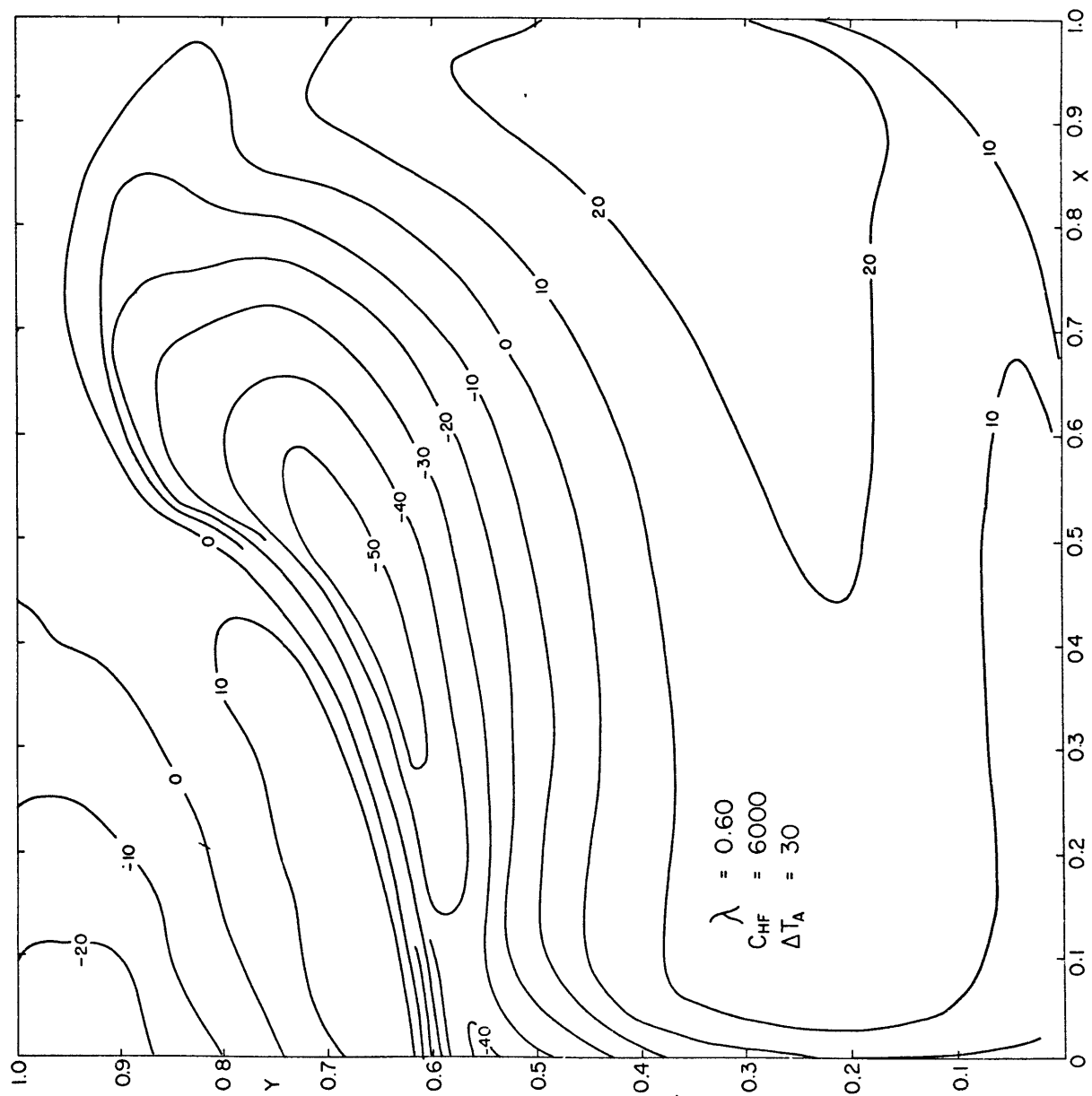**Fig. 11g.** Equilibrium Vertical Heat Flux in kcal cm^{-2} yr^{-1} (Case 7)

Fig. 11h. Equilibrium Vertical Heat Flux in $\text{kcal cm}^{-2}\text{ yr}^{-1}$ (Case 8)

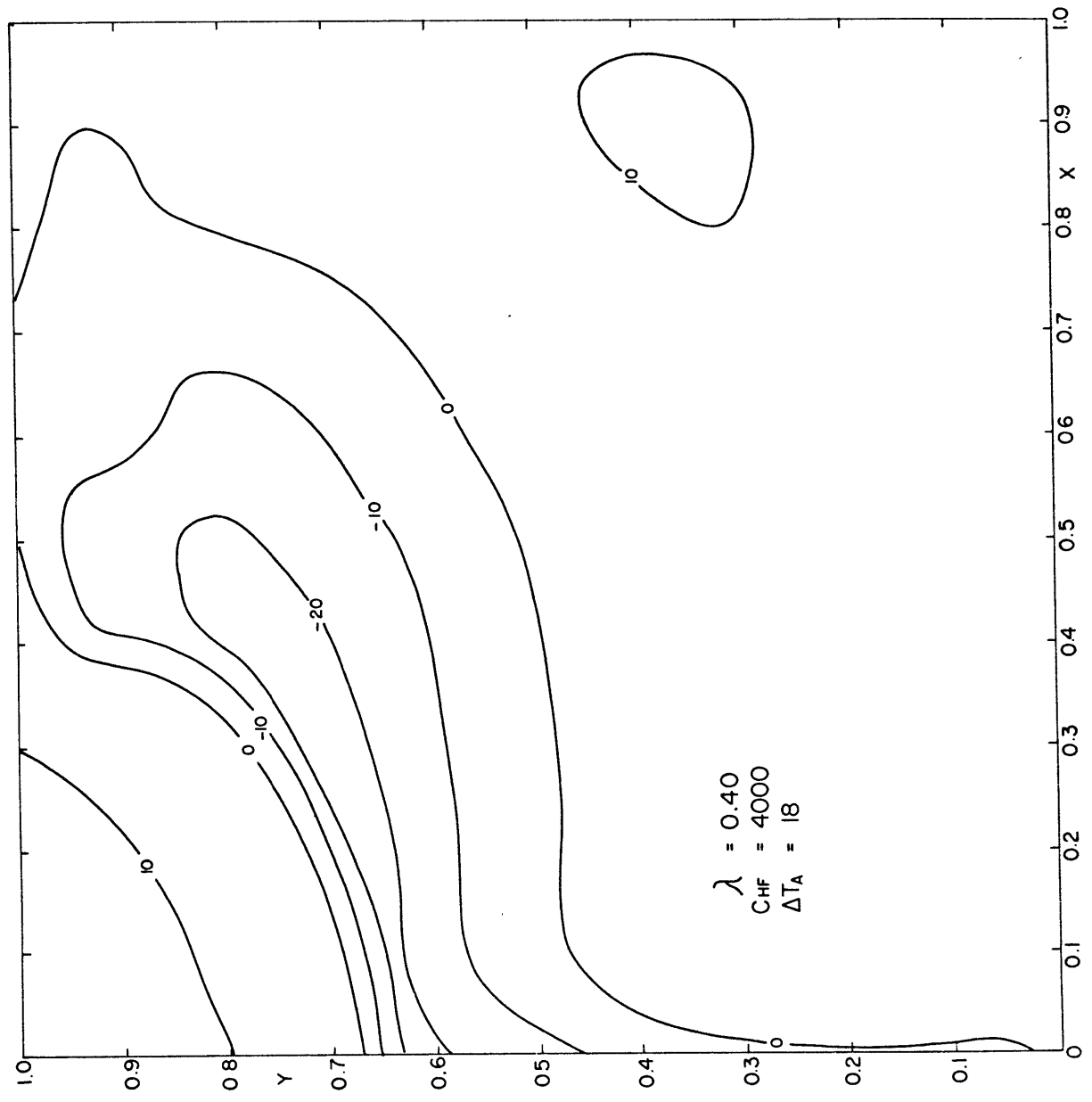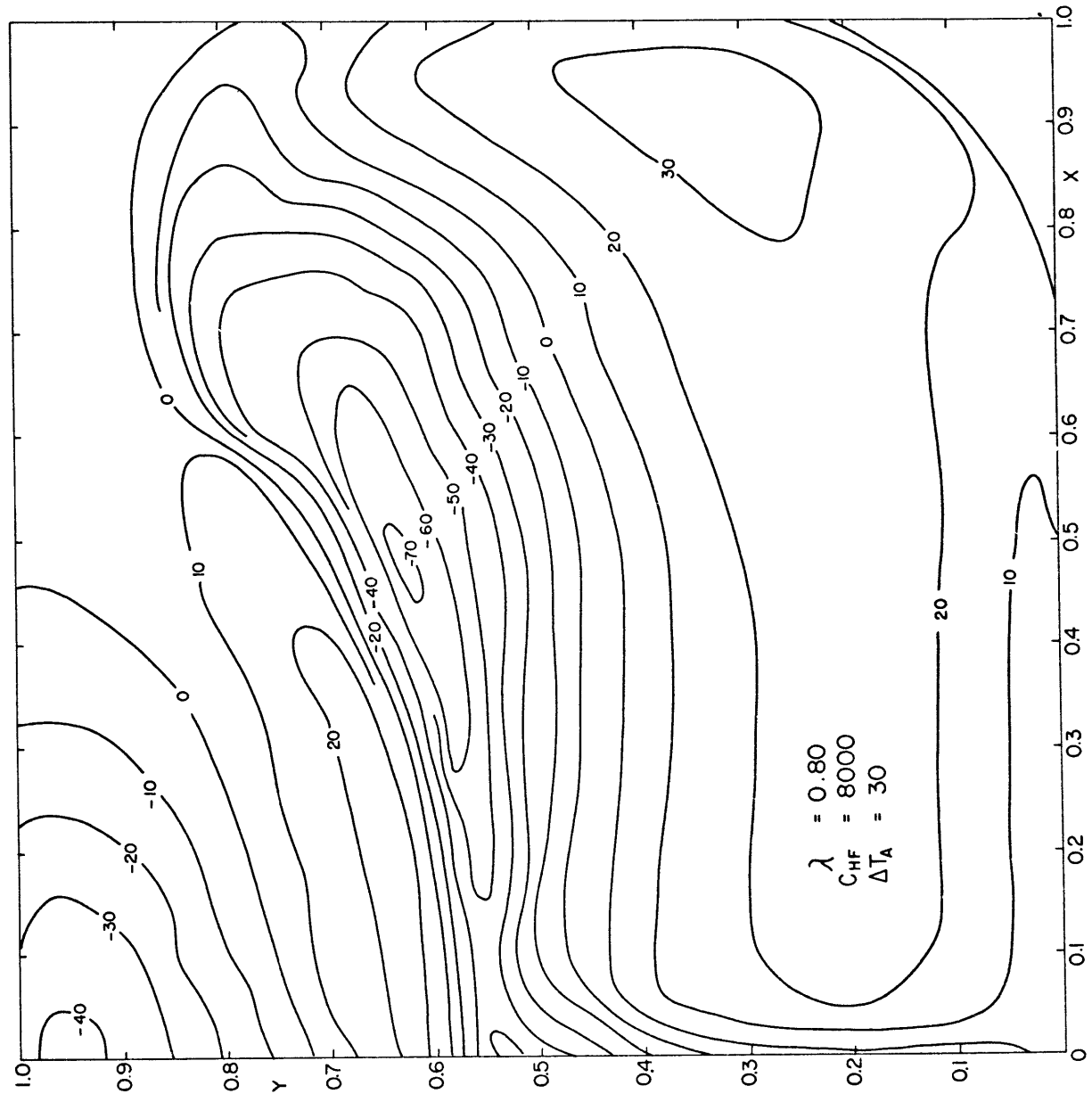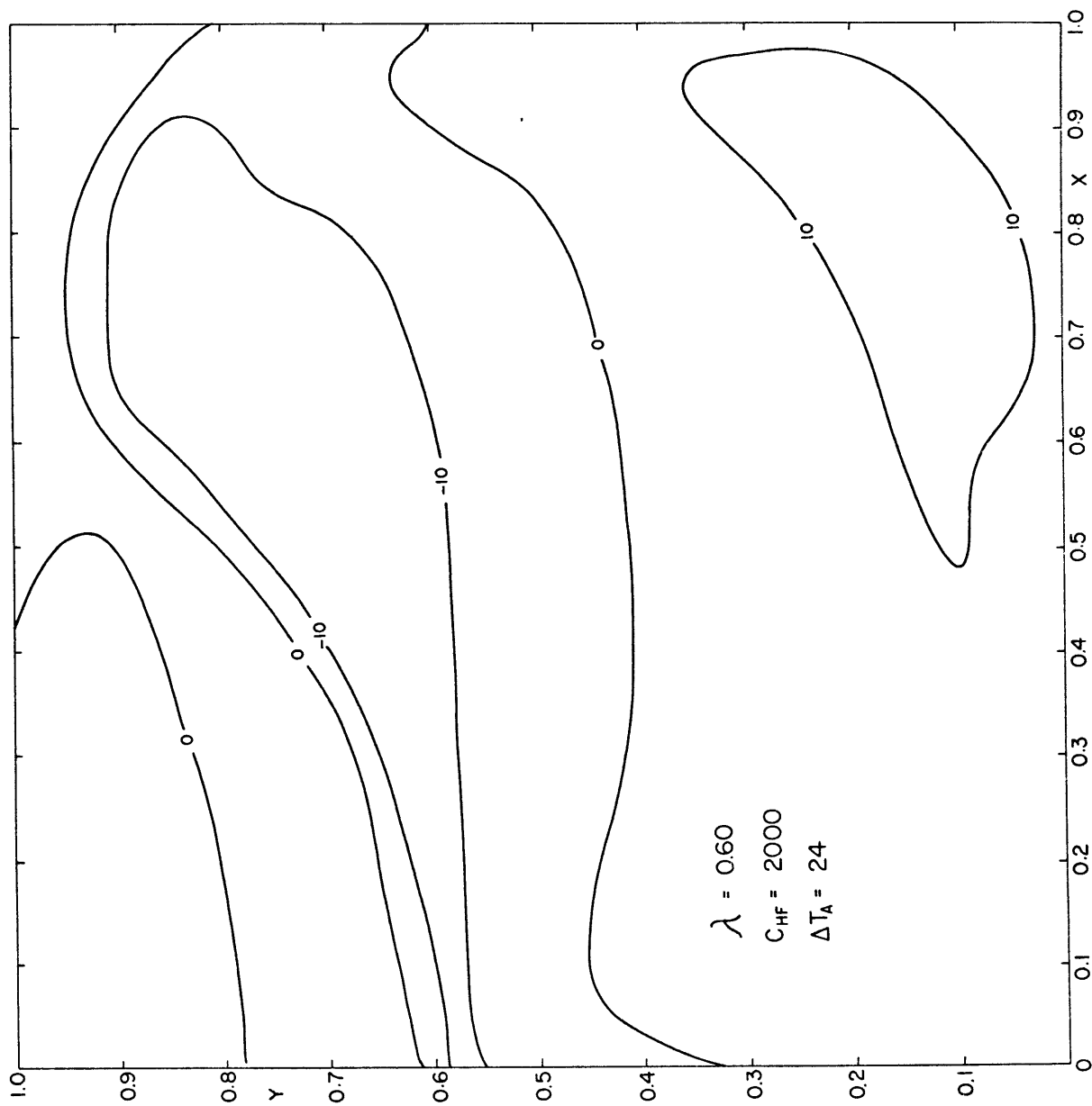**Fig. 11i.** Equilibrium Vertical Heat Flux in kcal cm^{-2} yr^{-1} (Case 9)

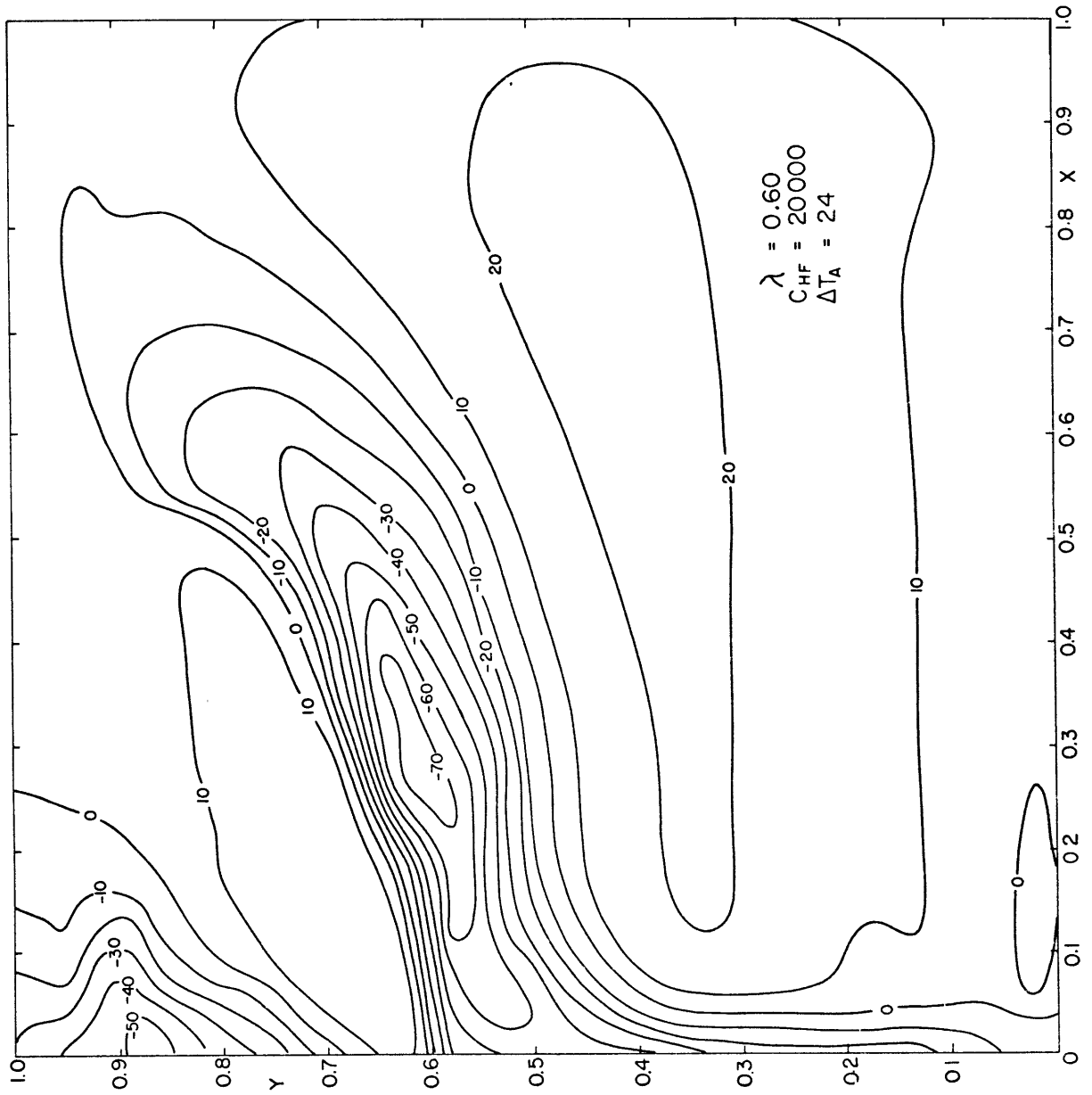**Fig. 11j.** Equilibrium Vertical Heat Flux in kcal cm^{-2} yr^{-1} (Case 10)

Fig. 11k. Equilibrium Vertical Heat Flux in kcal cm^{-2} yr^{-1} (Case 11)

used similar parameterizations for the vertical heat flux.
The standard values for C_{HF} we used (4000 cal cm^{-2} yr^{-1}
°C$^{-1} \leq C_{HF} \leq$ 8000 cal cm^{-2} yr^{-1} °C^{-1}) are within the range
assumed in these studies and have the same percentage
variation as our values of λ.

The equilibrium balance is between horizontal advection
of heat and vertical transfers to the atmosphere. Comparing
Figs. 8b and 9a, it is seen that in the southeastern half
of the basin the equilibrium oceanic temperatures are
quite reflective of the overlying atmospheric temperatures,
with the pattern slightly shifted in the flow direction. In
the remainder of the basin there is a significant deviation
from the overlying temperatures as a consequence of the
strong heat advection in the boundary currents.

On crossing the line of separation the sense of the
heat advection reverses. This increases the intensity of
the front which primarily develops in the upper layer due
to the differential heat advection between the core of the
boundary current and the slower moving water towards the line
of separation.

Figs. 10a and 10b, taken from the U.S. Naval Oceano-
graphic Atlas show sea surface temperatures in the North
Atlantic for the month along the western boundary, and the
predominantly zonal character of the isotherms in the central
part of the basin. Fig. 9a compares less well with the
August sea surface temperatures in Fig. 10b. The observed

predominantly zonal temperature gradient in the south-
eastern North Atlantic in summer cannot be likened to any
feature in Fig. 9a.

Corresponding to the temperature distributions in
Figs. 8b and 9a is the equilibrium vertical heat flux from
the atmosphere to the ocean according to the linear heat
flux law, given in Fig. 10a. In the vicinity of the
boundary currents there is a strong heat flow to the
atmosphere. In the majority of the basin there is a weak
heat flow into the ocean. The distribution is similar to
that of Fig. 12b from Bunker and Worthington (1976) which
was calculated from climatological data using aerodynamic
transport laws. Bunker and Worthington included the
effects of atmospheric stability in their drag coefficients,
greatly enhancing the vertical flux in the Gulf Stream
region. We do not take stability into account. Budyko's
(1963) distribution in Fig. 12a was derived with no consider-
ation of stability. This helped to weaken the intense Gulf
Stream feature in his results.

Figs. 9b, 9c and 11b, 11c show the effects of first
increasing and then decreasing the heat flux constant. This
effectively increases and then decreases the ratio of vertical
transfers to advection. In the high constant case (Case 2),
the temperatures in the ocean interior are more represent-
ative of the overlying atmospheric temperatures and the warm

water tongue has less of a northward penetration than in
Case 3, the low constant case. The vertical heat fluxes
are stronger in Case 2 than in Case 3 and the maximum is
displaced slightly further upstream.

Cases 4 (Figs. 9d, 11d) and 5 (Figs. 9e, 11e) use
higher and lower values of the wind stress parameter than
the control. In these runs there are changes in the geometry
as well as changes in the local ratio of vertical transfers
to advection. The high wind stress case (Case 4) is
characterized by a stronger warm water tongue which extends
further to the north and east than in the low wind stress
case (Case 5). The greater eastward penetration of the
warm tongue is due to the more east-west orientation of
the line of separation near the separation point in Case 4
coupled with the greater particle velocities. The equi-
librium vertical fluxes are greater in magnitude in Case 4
and the area of negative values (heat transfer out of the
ocean) is larger than in Case 5.

Cases 6 (Figs. 9f, 11f) and 7 (Figs. 9g, 11g) present
results using the weak and strong gradient atmospheric
temperature distributions. These cases are primarily shown
for visual comparisons with other results. Because our
thermodynamic equation is linear in the temperature, changing
the gradient of temperature will only change the equilibrium
temperature gradients and vertical heat fluxes by a propor-
tionate amount.

Cases 8 (Figs. 9h, 11h) and 9 (Figs. 9i, 11i) are composite runs intended to explore the extreme behavior of the model with values of the parameters examined in isolation above. We combined the parameters which gave the highest and the lowest values of the equilibrium heat flux. With certain qualifications.these cases might be identified with perpetual summerlike (Case 8) and winter-like (Case 9) atmospheric conditions. In winter the stronger gradients and winds (greater λ). These stronger atmospheric winds coupled with the decreased atmospheric gravitational stability due to the relatively warmer oceans would lead to stronger turbulent heat transfers at the air-sea interface (greater heat flux constant). Neglect of seasonal changes in oceanic heat storage capability might invalidate this argument.

Cases 8 and 9 do exhibit the smallest and the largest magnitudes of equilibrium vertical heat flux. If we compare Figs. 9h with 10b and 9i with 10a certain properties of the observed seasonal change in sea surface temperature do seem evident in the model results. Among these are the stronger overall gradient in winter and the larger meridional extent of isotherms on the eastern side (northeastern in the model).

As realistic values of the heat flux constant are some-what difficult to determine, we present Cases 10 (Figs. 9j, 11j) and 11 (Figs. 9k, 11k) in which this parameter has been

varied over a wider range than in Cases 2 and 3. For high C_{HF} the tongue of warm water is strongly suppressed. For low C_{HF} the isotherms on the eastern side of the basin have a large north-south extent.

Fig. 13 shows the northward flux of heat across a latitudinal wall in the basin for Case 1. The barriers at the furthest meridional extents of the basin force the heat flux to vanish there. The model values of the northward heat flux are of the same order of magnitude as present observational estimates for the world ocean (cf. Oort and Vonder Haar, 1976).

Fig. 14 shows the northward heat flux as a function of latitude and wind stress. In the active center region we see an interesting progressive change in the northward flux distribution as λ increases from 0.35 to 0.85. The north side of the peak becomes increasingly squeezed towards the center as the area of surfaced lower layer increases. The peak fluxes increase for low values of λ and then gradually decrease. Depending on the latitude and the value of λ an increase in the wind stress driving may lead to either an increase or a decrease in the oceanic heat flux. This has relevance to the feedback in the atmosphere-ocean dynamical system in which changes in oceanic heat transports due to changes in wind driving modify the energy supply for the atmospheric circulation. Fig. 14 shows that for our model this feedback has both positive and negative values

NORTHWARD HEAT FLUX $(10^{13}$ W)

$\lambda = 0.60$

$C_{HF} = 6000$

$\Delta T_A = 24$

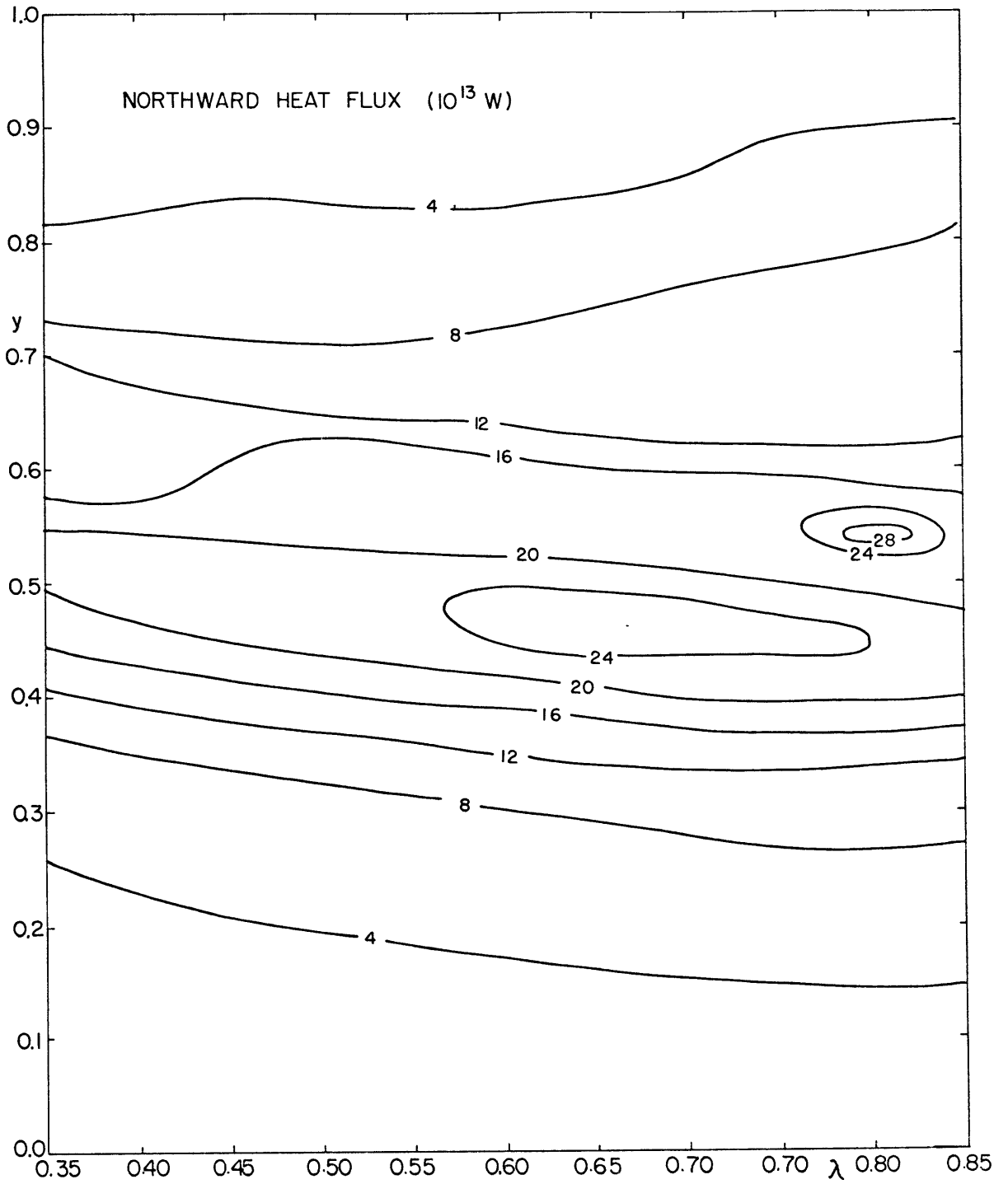Fig. 13. Equilibrium Northward Heat Flux vs. latitude for Case 1.
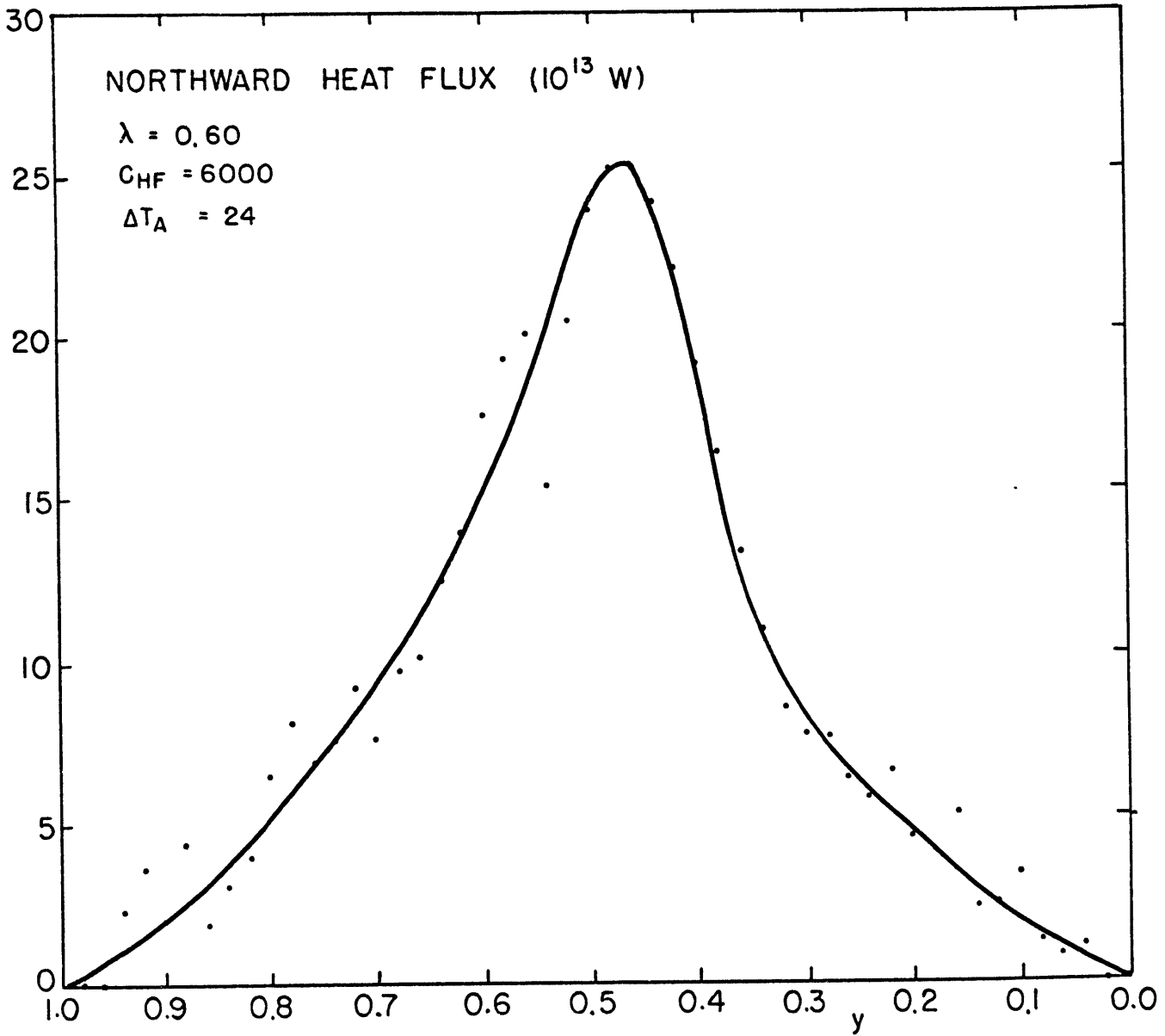
Fig. 14. Equilibrium Northward Heat Flux vs. latitude
          and λ

in different regions of parameter space.

We have also tested the sensitivity of the northward heat flux to the heat flux constant and meridional temperature gradient. Fig. 15 shows the northward flux as a function of y and C_{HF}. For the values of C_{HF} chosen the northward flux increases with C_{HF} . As C_{HF} becomes very large (outside of the range of values presented) the ocean temperatures approach the atmospheric temperatures and for our zonally uniform distribution of atmospheric temperatures the northward flux goes to zero. Fig. 16 gives the northward flux as a function of y and ΔT_A . There is a linear increase in the flux with ΔT_A due to the linear nature of the thermodynamic equation.
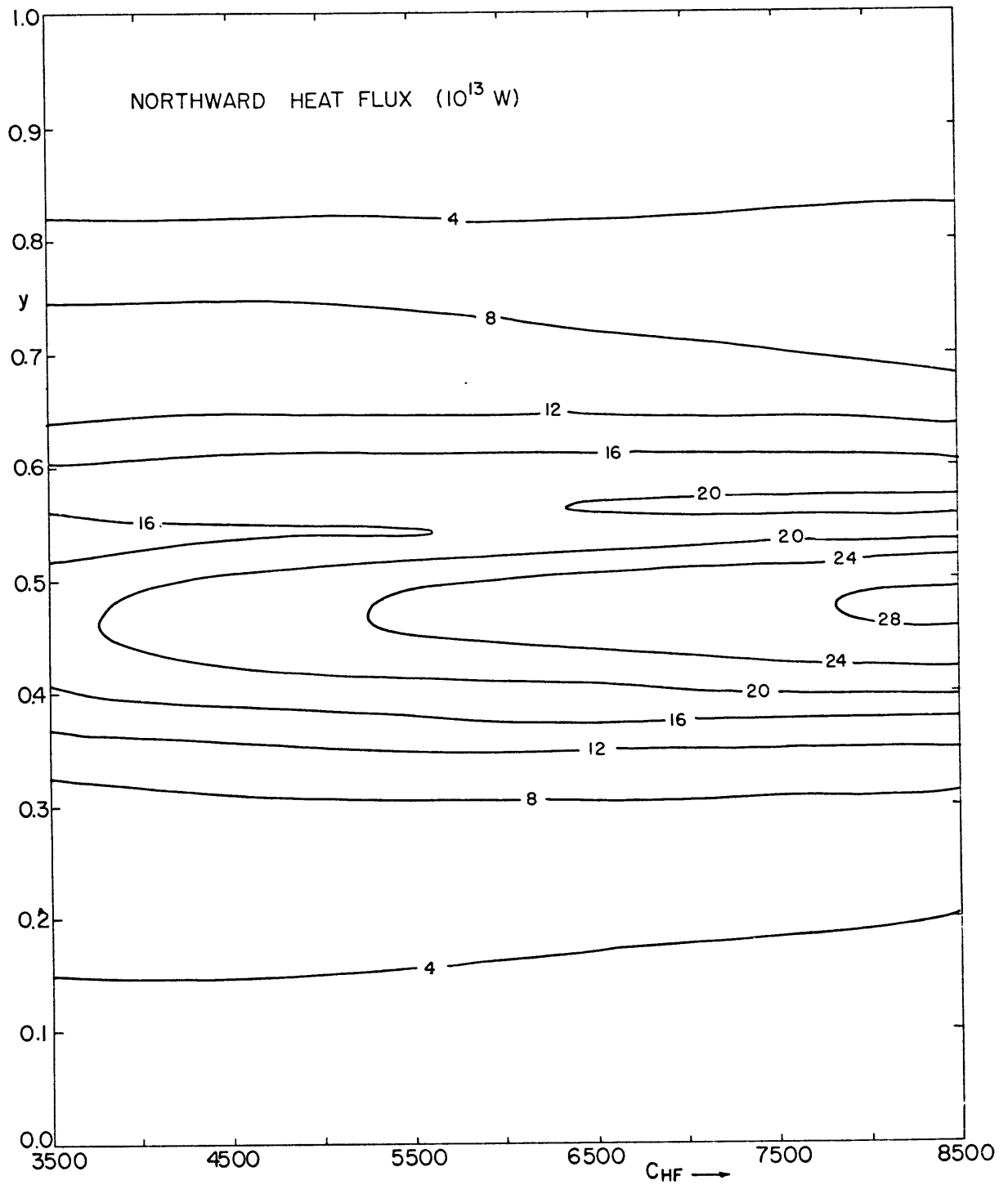
Fig. 15. Equilibrium Northward Heat Flux vs. latitude and C_{HF}
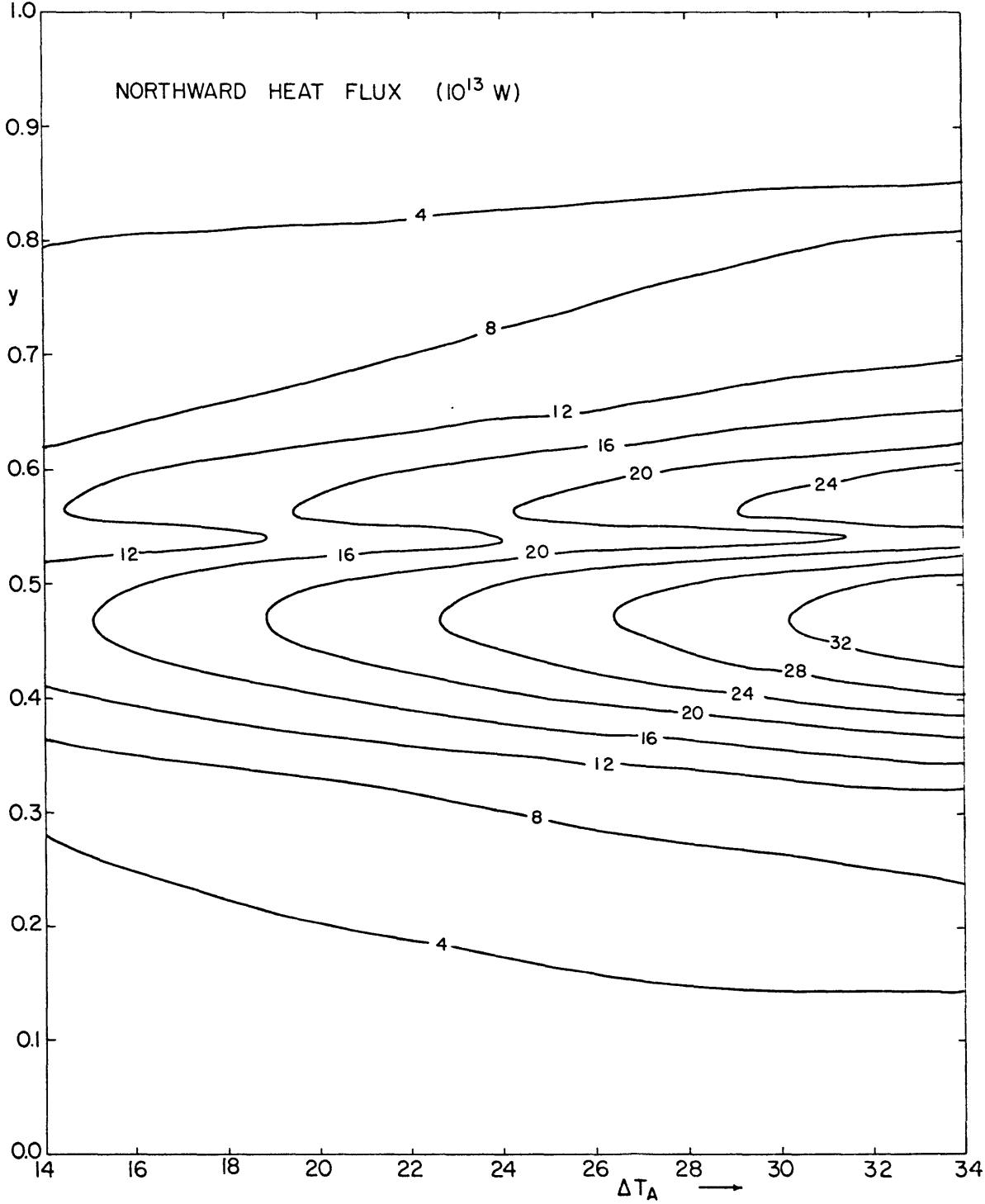
Fig. 16. Equilibrium Northward Heat Flux vs. latitude
and ΔT_A

V. Conclusions

We have presented results from a simple model of air-sea interaction. Atmospheric boundary conditions for the ocean model were idealized and held fixed. The large-scale steady-state ocean circulation was calculated. A Lagrangian temperature integration was performed to find the steady-state temperatures of the ocean surface layer. Vertical and northward heat fluxes were calculated.

Significant qualitative agreement was found between calculated results and observations, particularly in the general patterns of the oceanic temperature and the vertical heat flux. The sensitivity of the model results to the external conditions was tested and perpetual seasons were simulated. The dependence of the model heat flux on the wind stress was examined. A large number of figures is presented to allow extensive visual intercomparisons of model results.

The major value of a study of this type would seem to be the insight it provides for understanding the basic processes involved in large-scale air-sea interaction. We have assumed a thermal balance of horizontal heat advection being counteracted by vertical heat tranfers. The qualitative agreement between the observed ocean temperatures and air-sea heat fluxes and the model results suggests that the major processes active have been sufficiently well

represented to give correct general patterns. We suggest
that the seasonal variations in the North Atlantic sea-
surface temperatures are due primarily to suppressed
vertical heat fluxes in summer due to increased stability.
For the Atlantic it seems clear that dynamic processes
are equally as important as vertical heat transfers at the
air-sea interface in determining the equilibrium sea surface
temperature patterns.

The variation of the model northward heat flux with
changes in the wind stress parameter suggest that, although
this is generally the case, there may not always be a
negative feedback between atmospheric wind driving of the
surface ocean circulation and resultant effects of heat
transports by these circulations on the atmospheric baro-
clinicity. Stong enough driving of the ocean leads to homo-
genization of the sea surface temperatures and reduction of
the northward heat transports despite stronger circulations.

This study leaves many questions unanswered due to the
extreme crudeness of the model. More sophisticated treat-
ments of oceanic heat storage and turbulent transfer between
the ocean and the atmosphere are needed to verify the
results even within this very limited-interaction framework.

APPENDIX

SOLUTIONS TO MODEL CIRCULATION EQUATIONS

$$\gamma = (\tau, 0) \qquad \gamma = -\cos(\pi y)$$

A. Interior - Upper Layer

$$\psi = \lambda(1-x)\,\tau_y \qquad (1)$$

$$D^2 = h^2 + 2\lambda(1-x)\,f^2\,(\tau/f)_y \qquad (2)$$

B. Western Boundary Layer - Upper Layer

$$D = D_1(1-Be^{-\eta})/(1+Be^{-\eta}) \quad (1) \qquad B = (D_1-D_0)/(D_1+D_0)$$

$$\psi = (D^2-D_0^2)/2f \quad (2) \qquad \eta = \frac{x D_1}{\epsilon}, \; D_0^2 = h^2 - 2\lambda\tau, \; D_1^2 = h^2 + 2\lambda f^2\left(\frac{\tau}{f}\right)_y$$

C. Separated Boundary Layer - Upper Layer

Line of Surfacing $\quad x = X(y) = 1 - \dfrac{h^2}{2\lambda\tau}$ (1) $\quad D_1^2 = \dfrac{h^2 f \tau_y}{\tau}$ (2)

$$D = D_1(1-e^{-\eta})/(1+e^{-\eta}) \quad (3) \qquad \eta = \frac{x f_s D_1}{\epsilon} \qquad \psi = \frac{D^2}{2f} \quad (4) \qquad f_s = \text{gradient of } f \text{ along line of separation}$$

D. Interior - Lower Layer

$$\psi' = \lambda'\,\tau_y\,(X-x) \qquad (1)$$

$$D'^2 = h'^2 + 2\lambda'(X-x)\,f^2(\tau/f)_y \qquad (2) \qquad D_1'^2 = h'^2 + 2\lambda'\,f^2(\tau/f)_y\,X$$

E. Western Boundary Layer - Lower Layer

$$D' = D_1'(1-B'e^{-\eta'})/(1+B'e^{-\eta'}) \qquad (1) \qquad \eta' = \frac{x D_1'}{\epsilon'}$$

$$B' = (D_1'-D_0')/(D_1'+D_0')$$

$$\psi' = (D'^2-D_0'^2)/2f \qquad (2) \qquad D_0'^2 = h'^2 - 2\lambda'\,\tau X$$

References

Bryan, K., S. Manabe and R. C. Pacanowski, 1975: A global ocean-atmosphere climate model. Part II. The oceanic circulation. J. Phys. Oceanogr., 5, 30-46.

Budyko, M. I., 1963: Atlas of the Heat Balance of the Earth. (In Russian) Moscow, Globnaia Geofiz. Observ., 69 pp.

Bunker, A. F., and L. V. Worthington, 1976: Energy exchange charts of the North Atlantic Ocean. Bull. Amer. Meteor. Soc., 57, 670-678.

Haney, R. L., 1971: Surface thermal boundary condition for ocean circulation models. J. Phys. Oceanogr., 1, 241-248.

Haney, R. L., 1974: A numerical study of the response of an idealized ocean to large scale surface heat and momentum flux. J. Phys. Oceanogr., 4, 145-167.

Kamenkovich, V. M., and G. M. Reznik, 1972: A contribution to the theory of stationary wind-driven currents in a two-layer liquid. Isv., Atmos. and Oceanic Phys., 8, 419-434.

Manabe, S., K. Bryan and M. Spelman, 1975: A global ocean-atmosphere climate model. Part I. The atmospheric circulation. J. Phys. Oceanogr. , 5, 3-29.

Oceanographic Atlas of the North Atlantic Ocean, Section II, Physical Porperties, 1967: U.S. Naval Oceanographic Office, Pub. No. 700, 300.pp.

Oort, A.H., and T.H. Vonder Haar, 1976: On the observed annual cycle in the ocean-atmosphere heat balance over the Northern Hemisphere. J. Phys. Oceanogr., 6, 781-800.

Parsons, A.T., 1969: A two-layer model of Gulf Stream
    separation. J. Fluid Mech., 39, 511-528.

Takano, K., 1975: A numerical simulation of the world ocean
    circulation. Preliminary results. Numerical Models of
    Ocean Circulation, Acad. of Sci. Washington, D.C.,
    121-1291

Veronis, G., 1973: Model of World Ocean Circulation: I.
    J. Mar.Res., 31, 228-288.

Vonder Haar, T.H., and A.H. Oort, 1973: New estimate of
    annual poleward energy transport by Northern Hemisphere
    oceans. J. Phys. Oceanogr., 2, 169-172.

Acknowledgements

final draft with style.

Thanks are due the NASA Goddard Laboratory for Atmospheric Science for the use of their computing facilities. I am also appreciative for financial support from the National Science Foundation under Grant Number NSF-g-76-20070 ATM during my three years at M.I.T.

Finally, I would like to acknowledge my family and the friends I have made in Boston without whom this work would not have been completed.